This is a repository copy of *Tuning Ligands Ratio Allows for Controlling Gold Nanocluster Conformation and Activating a Nonantimicrobial Thiol Fragrance for Effective Treatment of MRSA-induced Keratitis*.

White Rose Research Online URL for this paper:
https://eprints.whiterose.ac.uk/201854/

Version: Accepted Version

Article:

Pang, Z., Ren, N., Wu, Y. et al. (6 more authors) (2023) Tuning Ligands Ratio Allows for Controlling Gold Nanocluster Conformation and Activating a Nonantimicrobial Thiol Fragrance for Effective Treatment of MRSA-induced Keratitis. Advanced Materials, 35 (40). 2303562. ISSN 0935-9648

https://doi.org/10.1002/adma.202303562

Tuning Ligands Ratio Allows for Controlling Gold Nanocluster Conformation and Activating a Nonantimicrobial Thiol Fragrance for Effective Treatment of MRSA-induced Keratitis

Zeyang Pang[§], Ning Ren[§], Yujie Wu, Jie Qi, Fupin Hu, Yuan Guo, Yangzhouyun Xie, Dejian Zhou* and Xingyu Jiang*

Dr. Z. Pang, Dr. N. Ren, Y. Wu, J. Qi, Dr. Y. Xie, Prof. X. Jiang

Shenzhen Key Laboratory of Smart Healthcare Engineering and Guangdong Provincial Key Laboratory of Advanced Biomaterials, Department of Biomedical Engineering, Southern University of Science and Technology, No 1088, Xueyuan Rd., Nanshan District, Shenzhen, Guangdong 518055, P. R. China

E-mail: jiang@sustech.edu.cn

Dr. Z. Pang, Prof. D. Zhou

School of Chemistry and Astbury Centre for Structural Molecular Biology, University of Leeds, Leeds LS2 9JT, United Kingdom

E-mail: d.zhou@leeds.ac.uk

Prof. Y. Guo

School of Food Science and Nutrition and Astbury Centre for Structural Molecular Biology, University of Leeds, Leeds LS2 9JT, United Kingdom

Prof. F. Hu

Institute of Antibiotics, Huashan Hospital, Fudan University, Shanghai 200040, P. R. China

$ These authors contributed equally to this work.

Abstract

Bacterial keratitis is a serious ocular disease that affects millions of people worldwide each year, among which ~25% are caused by *Staphylococcus aureus.* With the spread of bacterial resistance, refractory keratitis caused by methicillin-resistant *Staphylococcus aureus* (MRSA) affects ~120–190 thousand people annually and has become a significant cause of infectious blindness. Atomically precise gold nanoclusters (GNCs) have recently emerged as promising antibacterial agents, although how GNC structure and capping ligands control its antibacterial properties remain largely unexplored. In this study, by adjusting the ratio of a "bulky" thiol fragrance to a linear zwitterionic ligand, the GNC conformation is transformed from $Au_{25}(SR)_{18}$ to $Au_{23}(SR)_{16}$ species, simultaneously converting both inactive thiol ligands into potent antibacterial nanomaterials. Surprisingly, mixed-ligand capped $Au_{23}(SR)_{16}$ GNCs exhibit superior antibacterial potency compared to their mono-ligand counterparts. The optimal GNC is highly potent against MRSA, showing >1024-fold lower minimum inhibitory concentration than the corresponding free ligands. Moreover, it displays excellent potency in treating MRSA-induced keratitis in mice with greatly accelerated corneal recovery (by ~9-fold). Thus, this study establishes a feasible method to synthesize antibacterial GNCs by adjusting the ligand ratio to control GNC

conformation and active non-antibacterial ligands, thereby greatly increasing the repertoires for combating multidrug-resistant bacterial infections.

1. Introduction

Bacterial keratitis, also known as corneal bacterial infection, is the leading cause of monocular blindness[1] and affects approximately 1.7 million people each year worldwide[2]. Bacterial keratitis may be caused by pathogens following mechanical injury to the cornea[3]. Even mild bacterial keratitis can cause corneal redness, swelling, and photophobia in patients[4]. Without timely and effective treatment, bacterial keratitis can lead to severe symptoms, including ulceration, corneal opacity, and eventually blindness, thereby seriously affecting the quality of life of patients[5]. Bacterial keratitis incidences have significantly increased in recent years due to the increased use of contact lenses worldwide[6]. The primary causative agent of bacterial keratitis is gram-positive bacteria, with *Staphylococcus aureus* implicated in over 25% of all cases[7]. In particular, bacterial keratitis caused by drug-resistant strains, such as methicillin-resistant *Staphylococcus aureus* (MRSA), has posed a major threat because of their high resistance against common ocular antibiotics[8]. The recurrent infections frequently necessitate surgical intervention, which can significantly compromise the quality of life for affected patients[2] [9]. As an important force against MRSA-induced keratitis, nanomaterials (including organic nanoparticles[10] such as polydopamine nanoparticles[11], inorganic nanomaterials such as carbon quantum dots[12], silver nanoparticles[13] [14], and organic-inorganic composites[15] [16]) have shown to be more effective than traditional antibiotics because they can offer multiple antibacterial mechanisms in one agent, making it difficult for bacteria to develop resistance. In addition, they can also offer other therapeutic functions, such as anti-inflammation[17],

3

to benefit treatment. However, the unpopularity of antikeratitis research and the limited therapeutic drugs have prompted us to search for a new generation of highly efficient nano-antibiotics.

Atomically precise gold nanoclusters (GNCs) have been widely used in biomedical research, including bone and tumor imaging[18] [19] [20] [21]; drug delivery[22]; biomarker detection[23]; anticancer[24] [25] [26], antiplasmodium[27], antiviral studies[28]; as well as bacterial infection detection and treatment[29] [30] [31]. By differing by just one to a few Au atoms in the chemical formula, GNCs exhibit significantly different electrochemical[32], optical[33], and catalytic properties[34], as well as distinct thermodynamic stabilities[35]. For example, changing the GNC structure from $Au_{25}(SR)_{18}$ to $Au_{23}(SR)_{16}$ (SR = thiolated ligand) has dramatically boosted its photoelectrochemical performance as a photosensitizer[36]. These findings underscore the significance of investigating the relationship between the GNC formula and its physicochemical properties. The interconversion of GNCs with different Au atomic numbers, especially between Au_{25} and Au_{23} NC, can be achieved by using excessive reducing agent[37], ligand etching[38], acidification of the solution[39], irradiation[40], and ligand exchange[41] [42]. Particularly, by controlling the ligand steric hindrance to peripheral ligands (bulkiness), significant interconversion between $Au_{23}(S\text{-}tBu)_{16}$ and $Au_{25}(SCH_2CH_2Ph)_{18}$ has been realized through ligand exchange[43] [44]. Based on our successful synthesis of dual-ligand-capped GNCs[45], we envisage that varying the ratio of two ligands with different steric hindrances may change the GNC conformation, allowing us to screen their conformation-dependent antibacterial properties.

Herein, we have explored this strategy by combining two ligands [a thiol fragrance, 4-mercapto-4-methyl-2-pentanol (4MMP), and a thiolated zwitterionic ligand (C5)] to achieve the transformation of $Au_{25}(SR)_{18}$ to $Au_{23}(SR)_{16}$ through adjusting the ligand

4

feed ratio (**Scheme 1**). 4MMP is a natural product[46] [47] [48] approved as a compliant food additive by World Health Organization[49] [50]. Similar to HS-tBu, the two methyl groups next to the thiol group in 4MMP pose a significant steric hindrance to peripheral ligands after capping (**Scheme 1**, marked with oval dotted line frames), favoring the formation of small GNCs like $Au_{23}(SR)_{16}$. The highly biocompatible zwitterionic ligand (C5) is employed as a spacer to adjust the 4MMP capping ligand density on GNC and to regulate its binding pattern with bacterial membranes[51]. In comparison, the linear structure of C5 is less bulkier than 4MMP at the GNC anchoring point, which favors the formation of big $Au_{25}(SR)_{18}$[52]. Indeed, our findings indicate that a gradual increase in the 4MMP ratio results in a conformational shift of GNC from $Au_{25}(SR)_{18}$ to $Au_{23}(SR)_{16}$. Notably, although both ligands exhibit no apparent antibacterial properties (MIC >2 mg mL^{-1}), GNCs prepared with 70%–90% 4MMP ligand feed (mainly Au_{23} NCs) exhibit strong antibacterial potency with a minimum inhibitory concentration (MIC) as low as 2 μg mL^{-1} against MRSA. This antibacterial potency is comparable to some antibiotics of last resort. Moreover, this dual-ligand-capped GNC effectively kills bacteria without inducing membrane rupture and leakage of bacterial content, similar to that of daptomycin (Dap), which can avoid excessive inflammation and overreaction of the immune system. In both *in vitro* and *in vivo* keratitis models, this GNC shows superior antibacterial potency over vancomycin without inducing significant toxic effects. Together, these results have demonstrated the potential of this dual-ligand GNC as an effective nanomedicine for treating MRSA-induced bacterial keratitis.

5
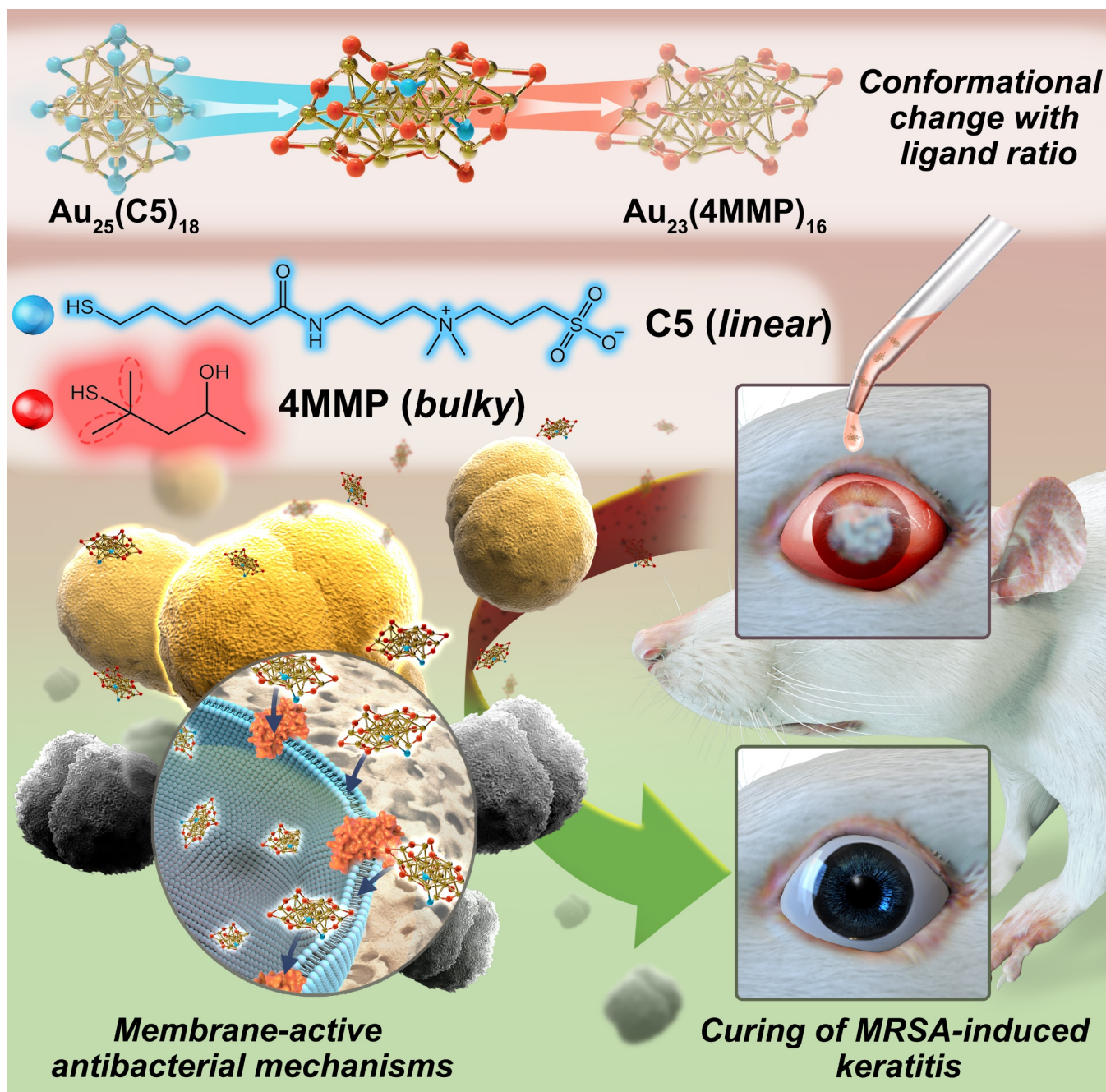
Scheme 1. Schematic diagram of this study. By controlling the feed ratio of two ligands, namely a thiolated zwitterionic ligand (C5, blue sphere represents thiol group in the ligand) and 4-mercapto-4-methyl-2-pentanol (4MMP, red sphere represents thiol group in the ligand), the conformation of the resulting GNC is changed from Au_{25} to Au_{23}, yielding >1024-fold higher antibacterial potency against MRSA than free ligands. The dual-ligand GNC induces the death of MRSA by affecting a series of physiological activities without causing bacterial membrane rupture. In a murine keratitis model, the

6

administration of GNC in the form of eye drops demonstrated exceptional therapeutic efficacy in terms of both MRSA clearance and the promotion of corneal recovery (Au atoms shown as golden spheres).

2. Results and discussion

By systematically increasing the 4MMP ligand feed ratio (from 0 to 100%) while maintaining a fixed total ligand (C5 + 4MMP)-to-Au ratio during GNC synthesis, we observed a clear change in the color of the solution from tea-brown to yellowish-green (**Figure 1A, left inset**). Given that each conformation of the GNC exhibits a distinct ultraviolet–visible (UV–vis) absorption spectrum, a change in GNC conformation was envisaged. The initial characteristic peak of Au_{25} NC at ~700 nm gradually flattened as the 4MMP feed was increased to 40%. Further increasing the 4MMP feed from 50% to 100%, a new absorption peak at ~600 nm appeared, along with a significant increase in the overall absorption intensity (**Figure 1A**). This shift is consistent with the change in GNC conformation from Au_{25} to Au_{23}, as reported previously[53] [54]. Moreover, the ratio of absorbance at 600 and 700 nm (A_{600}/A_{700}) exhibited a positive correlation with the proportion of 4MMP (**SI, Figure S1**), implying a gradual increase of the Au_{23}-to-Au_{25} NC ratio in the product.

The fluorescence excitation spectra of GNC with a 50% 4MMP feed ratio showed a broad absorption peak from ~650 nm to 800 nm (**SI, Figure S2A**). The fluorescence emission spectrum for pure C5-capped-GNC peaked at ~1080 nm under 808 nm laser excitation. As the proportion of 4MMP increased, the emission peak blue shifted to the short wavelength region (**SI, Figure S2B**). Interestingly, with the increasing 4MMP ratio, the NIR fluorescence of the resulting GNC solution was weakened. This observation aligns with the gradual transformation of strongly NIR fluorescent Au_{25}

7

into weakly NIR fluorescent Au_{23} NCs, implying that increasing the ratio of the bulkier 4MMP ligand changes the conformation of produced GNCs (**SI, Figure S2B, right inset**)[55] [56].

The morphology of GNCs was visualized under a double spherical aberration-corrected transmission electron microscope (TEM) with a high-angle annular dark-field model (**Figure 1B**). We statistically analyzed the size distribution of GNCs prepared under different 4MMP ratios (**Figure 1C**). The mean size of all dual-ligand GNCs was ~1.22 ± 0.10 nm. Despite a slight reduction in the mean size of GNCs from 1.28 to 1.15 nm as the 4MMP feed ratio increased, it was observed that the overall size distributions remained largely unchanged. To obtain the exact ligand contents with different feeds, we applied iodine to dissolve the Au kernel and analyzed the supernatant composition by integrating the characteristic peaks using the ^{1}H NMR spectrum[57]. Analysis of the relationship between the 4MMP percentage in the product and the 4MMP feed ratio revealed that the majority of the product line was situated above the theoretical line (**Figure 1D** and **SI, Figure S3**). This suggests that the proportion of 4MMP ligand in the GNC capping exceeded that in the feed (ratio of 20%–80%), suggesting a higher binding affinity of the 4MMP ligand towards the gold kernel than the C5 ligand.
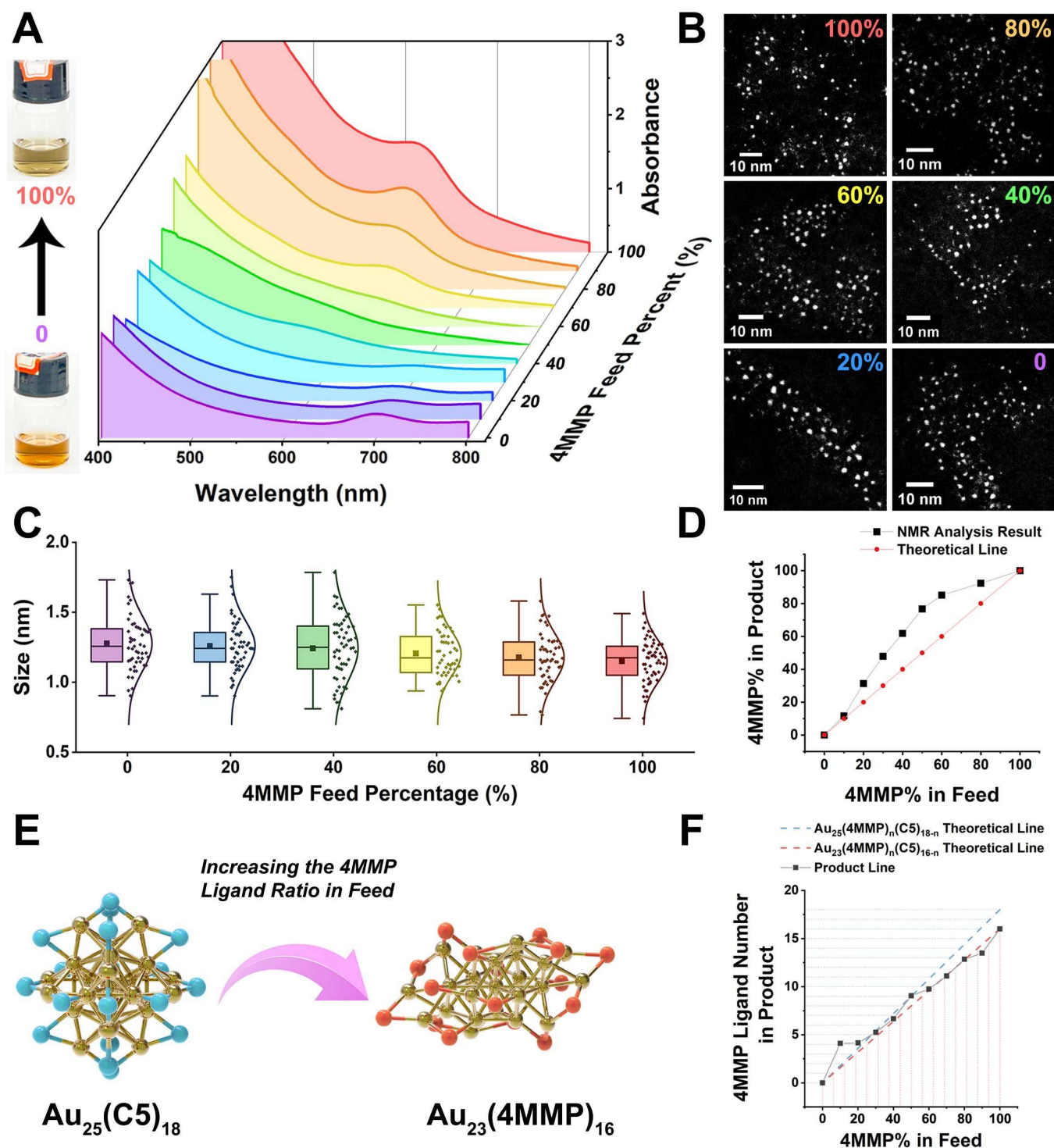
Figure 1. Characterization of the 4MMP-C5 dual-ligand-capped GNCs. (A) UV–vis spectra of GNCs prepared with 4MMP feed ratio ranging from 0 to 100%. The characteristic absorption peak showed a blue shift from ~700 to ~600 nm with the increasing 4MMP ligand feed, indicating a gradual change in the GNC conformation.

9

(Left inset: the ambient light image of GNCs with 4MMP feed ratios of 0 and 100%) (B) Double spherical aberration-corrected transmission electron microscopy images and (C) the corresponding size statistic boxplot of GNCs prepared with varying 4MMP ligand feeds. The mean size of GNCs shows a slight decrease from 1.28 to 1.15 nm as the 4MMP feed ratio increases from 0 to 100%. (D) ^{1}H NMR analysis reveals the relationship between the 4MMP ligand in feed and that in the product after the digestion of GNCs. (E) Schematic diagram showing the conformational change of GNCs from $Au_{25}(C5)_{18}$ to $Au_{23}(4MMP)_{16}$ with increasing 4MMP feed ratio from 0 to 100% (blue sphere: the thiol group of C5 ligand, red sphere: the thiol group of 4MMP ligand, and golden sphere: Au atom). (F) Calculated relationship between the 4MMP ligand feed and the number of 4MMP ligands in the product. The red line indicates $Au_{23}(SR)_{16}$ configuration, whereas the blue line indicates $Au_{25}(SR)_{18}$ configuration.

To characterize the conversion of GNC species with different 4MMP feeds, we calculated the molecular weight (MW) of $Au_{25}(SR)_{18}$ and $Au_{23}(SR)_{16}$ (**SI, Table S1**) and measured their mass spectra via electrospray ionization mass spectrometry (ESI–MS) (**SI, Figure S4**). After mass deconvolution, the MWs of the products were compared with those of calculated Au_{25} or Au_{23} NCs to determine the exact GNC species (**Table 1**). The Au_{23} NCs were labeled in blue for clear visualization of the structural shift in GNC composition. Utilization of 100% C5 ligand resulted exclusively in the formation of $Au_{25}(C5)_{18}$. As the 4MMP ligand feed increased from 0 to 20%, Au_{25} NCs remained the predominant product due to the inhibitory effect of the majority C5 ligand on the formation of Au_{23} NCs. However, when the 4MMP feed continued to increase from 30% to 70%, the number of 4MMP ligands on GNCs increased from 4 to 12 and gradually constituted the major ligands. Further increasing the 4MMP ligand ratio produced only Au_{23} NCs, most likely due to the steric hindrance of the now

10

majority 4MMP ligand inhibited the formation of Au_{25} NCs. A pure product of $Au_{23}(4MMP)_{16}$ was obtained when the 4MMP ligand feed reached 100%, thus achieving a complete transformation from Au_{25} to Au_{23} NC (**Figure 1E**). By graphically representing the relationship between the 4MMP ligand feed ratio and the number of 4MMP ligands present in the product (**Figure 1F**), it was possible to visualize the conversion of GNC species through comparison with the expected theoretical product lines for pure Au_{25} (blue) and Au_{23} (red) NCs. For 4MMP feeds ranging from 0 to 50%, the product line was closely aligned with the theoretical line for Au_{25} NCs. However, for 4MMP feeds ranging from 50% to 100%, the product line shifted towards the theoretical line for Au_{23} NCs. The Au 4f orbital X-ray photoelectron spectroscopy (XPS) peak of GNCs has been shown to shift to the lower binding energy region with the increasing GNC size; thus, it is a useful indicator to demonstrate changes in the GNC core structure[58]. We characterized the Au 4f orbitals of GNCs with 0 and 100% 4MMP feed ratios using XPS and observed a clear binding energy increase of ~0.23 eV, proving that with the increase of the proportion of 4MMP ligand, the overall GNC size was reduced (**SI, Figure S5**). In addition, the peak positions and offsets of Au $4f_{7/2}$ and $4f_{5/2}$ were similar to the previously reported interconversion of Au_{25} to Au_{23}[38]. Together, these data indicate the successful shift of GNC species from $Au_{25}(C5)_{18}$ to $Au_{23}(4MMP)_{16}$ with the increasing 4MMP ligand feed, which provides a solid basis for subsequent screening of the optimal antibacterial GNC.

Table 1. Summary of the molecular formulas of GNCs prepared with different 4MMP ligand feeds (Au_{23} NCs marked in blue) determined using ESI–MS. The relative abundance of different GNC species in each group is presented in descending order from top to bottom.

4MMP feed (%)	MW range (Da)	Main species	Secondary species
0	11379	$Au_{25}(C5)_{18}$	–
10	10069–11278	$Au_{25}(4MMP)_4(C5)_{14}$ $Au_{25}(4MMP)_3(C5)_{15}$ $Au_{25}(4MMP)_5(C5)_{13}$	$Au_{25}(4MMP)_2(C5)_{16}$ $Au_{25}(4MMP)_1(C5)_{17}$ $Au_{25}(4MMP)_6(C5)_{12}$
20	9661–11256	$Au_{25}(4MMP)_5(C5)_{13}$ $Au_{25}(4MMP)_6(C5)_{12}$ $Au_{25}(4MMP)_3(C5)_{15}$ $Au_{25}(4MMP)_2(C5)_{16}$	$Au_{25}(4MMP)_4(C5)_{14}$ $Au_{25}(4MMP)_1(C5)_{17}$ $Au_{23}(4MMP)_3(C5)_{13}$ $Au_{23}(4MMP)_2(C5)_{14}$
30	9221–11713	$Au_{25}(4MMP)_4(C5)_{14}$ $Au_{25}(4MMP)_3(C5)_{15}$ $Au_{25}(4MMP)_5(C5)_{13}$ $Au_{23}(4MMP)_4(C5)_{12}$	$Au_{25}(4MMP)_6(C5)_{12}$ $Au_{23}(4MMP)_5(C5)_{11}$ $Au_{23}(4MMP)_3(C5)_{13}$
40	8651–11035	$Au_{23}(4MMP)_3(C5)_{13}$ $Au_{25}(4MMP)_5(C5)_{13}$ $Au_{23}(4MMP)_4(C5)_{12}$ $Au_{23}(4MMP)_5(C5)_{11}$	$Au_{23}(4MMP)_2(C5)_{14}$ $Au_{25}(4MMP)_3(C5)_{15}$ $Au_{25}(4MMP)_6(C5)_{12}$ $Au_{25}(4MMP)_7(C5)_{11}$ $Au_{23}(4MMP)_6(C5)_{10}$ $Au_{23}(4MMP)_7(C5)_9$
50	8211–10127	$Au_{23}(4MMP)_6(C5)_{10}$ $Au_{23}(4MMP)_7(C5)_9$ $Au_{25}(4MMP)_{10}(C5)_8$ $Au_{25}(4MMP)_9(C5)_9$	$Au_{25}(4MMP)_8(C5)_{10}$ $Au_{23}(4MMP)_9(C5)_7$ $Au_{23}(4MMP)_8(C5)_8$ $Au_{25}(4MMP)_7(C5)_{11}$
60	8104–10281	$Au_{23}(4MMP)_8(C5)_8$ $Au_{23}(4MMP)_9(C5)_7$ $Au_{23}(4MMP)_7(C5)_9$ $Au_{25}(4MMP)_{10}(C5)_8$	$Au_{25}(4MMP)_9(C5)_9$ $Au_{25}(4MMP)_6(C5)_{12}$ $Au_{25}(4MMP)_5(C5)_{13}$ $Au_{23}(4MMP)_{10}(C5)_6$
70	7583–10016	$Au_{23}(4MMP)_{12}(C5)_4$ $Au_{25}(4MMP)_{12}(C5)_6$	$Au_{25}(4MMP)_9(C5)_9$ $Au_{25}(4MMP)_8(C5)_{10}$ $Au_{23}(4MMP)_{11}(C5)_5$

80	7140–8827	Au$_{23}$(4MMP)$_{13}$(C5)$_3$	Au$_{23}$(4MMP)$_{12}$(C5)$_4$ Au$_{23}$(4MMP)$_{14}$(C5)$_2$ Au$_{25}$(4MMP)$_{12}$(C5)$_6$
90	7186–7409	Au$_{23}$(4MMP)$_{14}$(C5)$_2$ Au$_{23}$(4MMP)$_{13}$(C5)$_3$	–
100	6746	Au$_{23}$(4MMP)$_{16}$	–

The minimum inhibitory concentration (MIC) and minimum bactericidal concentration (MBC) of dual-ligand GNCs prepared with varying 4MMP feeds are summarized in **Tables 2** and **3**, respectively. Seven gram-positive and -negative pathogens were tested, including the common dermal and soft-tissue infective pathogens (*Staphylococcus aureus* [*S. a*], *Staphylococcus epidermidis* [*S. e*], and *Staphylococcus hemolyticus* [*S. h*]), urinary tract infection and sepsis pathogens (*Enterococcus faecalis* [*E. f*], *Escherichia coli* [*E. c*], and *Pseudomonas aeruginosa* [*P. a*]), and the pneumonia pathogen *Klebsiella pneumoniae* (*K. p*). Their antibacterial effects are displayed using a color scale, with green indicating low MIC or MBC (high antibacterial potency) and red indicating the opposite.

Table 2. MIC of GNCs prepared with different 4MMP feed ratios against seven gram-positive and -negative pathogens (unit: $\mu g\ mL^{-1}$)

4MMP feed (%)	Gram-positive				Gram-negative		
	S. a	*S. e*	*S. h*	*E. f*	*E. c*	*P. a*	*K. p*
0	>256	>256	>256	>256	>256	>256	>256
10	>256	>256	>256	>256	>256	>256	>256
20	>256	>256	>256	>256	>256	>256	>256
30	>256	>256	>256	>256	>256	>256	>256
40	16	16	128	256	>256	>256	>256
50	16	16	16	128	128	32	128

60	8	8	16	32	64	32	128
70	4	4	8	8	64	32	128
80	4	4	8	4	128	32	128
90	4	4	8	8	128	64	128
100	16	16	16	32	128	128	128

Table 3. MBC of GNCs prepared with different 4MMP feed ratios against seven gram-positive and -negative pathogens (unit: $\mu g\ mL^{-1}$)

4MMP feed (%)	Gram-positive				Gram-negative		
	S. a	S. e	S. h	E. f	E. c	P. a	K. p
0	>256	>256	>256	>256	>256	>256	>256
10	>256	>256	>256	>256	>256	>256	>256
20	>256	>256	>256	>256	>256	>256	>256
30	>256	>256	>256	>256	>256	>256	>256
40	>256	>256	>256	>256	>256	>256	>256
50	32	32	64	256	256	64	256
60	32	32	32	64	256	64	256
70	8	16	16	16	256	64	256
80	8	16	16	16	256	64	256
90	8	8	16	16	256	128	256
100	64	64	128	128	>256	256	256

Horizontally, GNCs co-capped with 4MMP and C5 showed higher antibacterial potencies against gram-positive strains than gram-negative ones (especially for *Staphylococcus* species). Further, a vertical comparison demonstrated that the antibacterial effects of GNCs varied significantly with the 4MMP ligand feeds. Here, the C5 ligand is used as a spacer to tune the 4MMP ligand density on the GNC. It is evident that GNCs prepared with pure C5 ligand (100% C5 in feed) display no measurable antibacterial activities (**Table 3**), which is consistent with the previously

14

reported results[52] [59]. The antibacterial potencies of GNCs initially increased with increasing 4MMP ligand feeds from 0 to 60%, which then plateaued and showed little change from 70% to 90%, with a low MIC of 4 µg mL^{-1} against *S. a*, *S. e*, and *E. f* (**Figure 2A**). Surprisingly, further increasing the 4MMP feed to 100% yielded GNCs with significantly lower antibacterial potencies than those prepared with 90% 4MMP. These results show that the 4MMP/C5 co-capped GNCs have high potencies against gram-positive pathogens. The optimal 4MMP feed is ~70%–90%, where the antibacterial potencies of the resulting GNCs are >64-fold higher than those prepared with the 4MMP feed of 0–40%. In contrast, the 4MMP or C5 ligand alone exhibited no obvious antibacterial potency (MIC >2048 µg mL^{-1}). Furthermore, our results indicate that simple mixtures of free thiol ligands and chloroauric acid exhibited no antibacterial activity (**SI, Table S2**). Most notably, our findings reveal that only when the GNCs were capped with both C5 and 4MMP ligands at specific ratios did they exhibit significant bactericidal activity. In doing so, we have successfully converted these non-antibacterial ligands into potent antibacterial agents.

With the rapid increase of bacterial antibiotic resistance globally, agents that can effectively control the infection of multidrug-resistant (MDR) pathogens are highly valuable[60]. Thus, we also tested our GNCs against MDR gram-positive strains, including MRSA, methicillin-resistant *S. epidermidis* (MRSE), MDR *S. haemolyticus*, and vancomycin-resistant *Enterococcus* (VRE). The trends in potency for GNCs against such resistant strains *vs*. 4MMP ligand ratio were very similar to antibiotic-sensitive strains. The antibacterial potency of GNCs gradually increased with the increasing 4MMP feed of 0–60%, which then plateaued within the feed of 70%–90% and finally decreased considerably with the feed further increased from 90% to 100% (**Figure 2B** and **SI, Tables S3** and **S4**). Notably, the 70%–90% 4MMP-fed GNC

15

demonstrated even higher potency against the MDR strains than their antibiotic-sensitive counterparts, with an impressively low MIC of 2 μg mL^{-1} against MRSA. Thus, co-capping GNC with both ligands has successfully converted these inactive ligands into highly potent anti-MRSA agents.
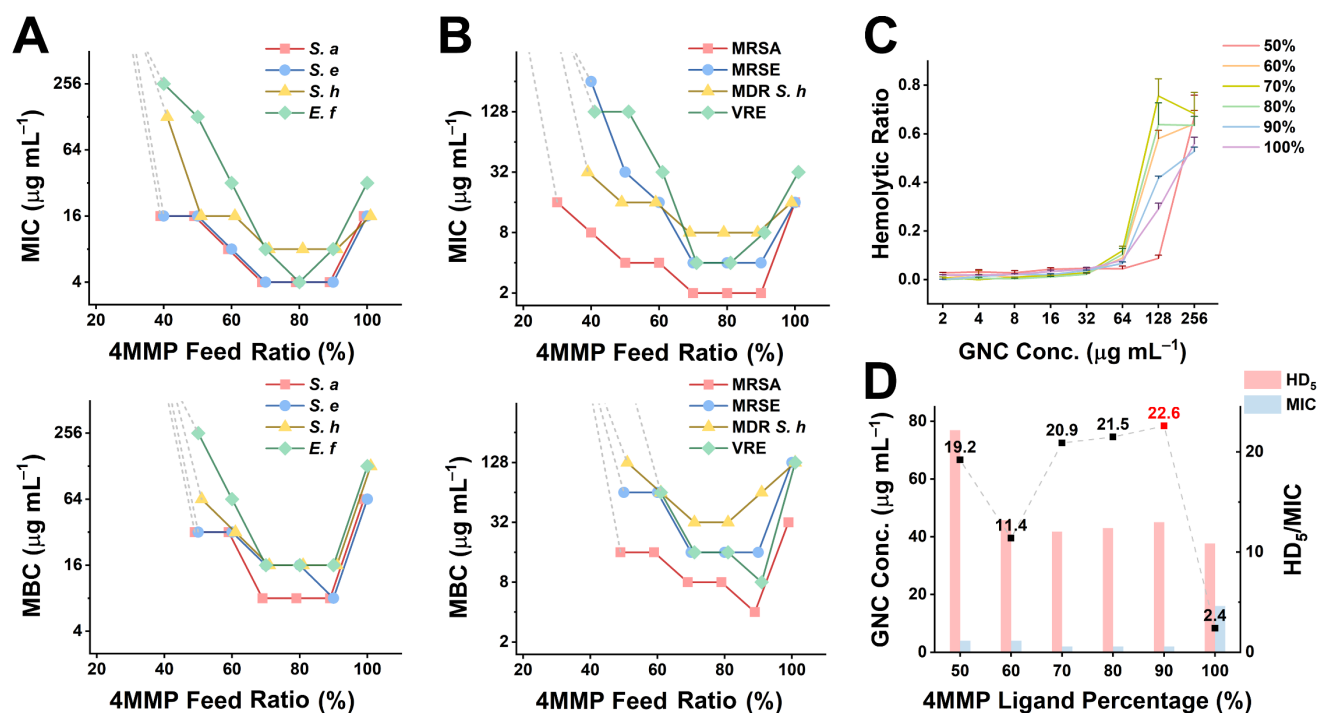

Figure 2. (A) The line plots showing the trends in MIC (top) or MBC (bottom) values for GNCs prepared with varying 4MMP ligand feed ratios against four gram-positive bacteria strains. All four strains exhibited a typical V-shaped curve, with the lowest MIC occurring at 4MMP feeds of 70%–90%. (B) The line plots showing the trends of MIC (top) or MBC (bottom) of GNCs prepared with different 4MMP ligand feed ratios against four MDR gram-positive bacterial strains. The MICs and MBCs of all GNCs against MRSA were lower than those against the antibiotic-sensitive *S. a* group. (C) The hemolytic ratio–concentration relationship of GNCs prepared with 4MMP ligand feed ratios of 50%–100%. The hemocompatibility rank was 70% <80% <60% <90%

<100% <50%. (D) The HD$_5$-to-MIC ratio of GNCs prepared with 4MMP ligand feeds of 50%–100% against MRSA. GNC prepared with a 4MMP feed of 90% showed the highest HD$_5$/MIC, demonstrating good antimicrobial efficacy and biosafety.

The above results have allowed us to draw two conclusions: 1) the antibacterial effect of the dual-ligand GNC is not linear with the 4MMP ligand ratio, and 2) the optimal bactericidal GNCs are obtained with 4MMP ligand at feeds of 70%–90%, which are mainly Au$_{23}$(SR)$_{16}$ species. We further investigated their hemocompatibility by incubating GNCs prepared with different 4MMP ligand ratios with 2% mouse red blood cell suspension. In general, all GNCs demonstrated a sharp increase in the hemolytic level at >64 µg mL^{-1} concentrations. However, a horizontal comparison revealed that the GNCs prepared with 4MMP feeds of 70% and 80% yielded higher hemolytic activity than other GNC species (**Figure 2C** and **SI, Figure S6**). An effective antibacterial agent should possess not only high antimicrobial potency (indicated by a low MIC value) but also exhibit excellent hemocompatibility (indicated by a high HD$_5$ value: the GNC dose giving 5% hemolysis). Thus, we calculated the HD$_5$/MIC ratio, an important indicator of the blood therapeutic window, to comprehensively determine the optimal GNCs (**Figure 2D**). Although the GNCs prepared with 4MMP feeds of 70%–90% demonstrated a high HD$_5$/MIC ratio of >20, those prepared with 90% 4MMP feed showed the highest HD$_5$/MIC ratio. Thus, this ligand ratio was deemed optimal for preparing antibacterial GNC in all subsequent analyses (hereafter denoted as **4MMP-GNC**). According to **Table 1**, the 4MMP-GNC prepared with 90% 4MMP feed corresponds to Au$_{23}$(SR)$_{16}$ with 13–14 4MMP and 2–3 C5 ligands. With a high HD$_5$/MIC ratio of ~23, its therapeutic window for treating gram-positive bacterial infections is wide and can be easily adjusted without worrying about hemolytic toxicity.

17

MRSA has high resistance to antibiotics of many different types and antimicrobial mechanisms[61]. We analyzed the resistance of the MRSA strains used in this study using several different classes of antibiotics, including macrolides, aminoglycosides, tetracyclines, glycopeptide, lipopeptide, quinolones, lincomycins, and chloramphenicol. Its corresponding MICs were evaluated and compared with that of 4MMP-GNC. Except for vancomycin (Van), erythromycin (Ery), and daptomycin (Dap), this MRSA strain demonstrated broad-spectrum resistance to all other antibiotics tested (**Table 4**). In contrast, the MIC of 4MMP-GNC (2 µg mL^{-1}) was significantly lower than most antibiotics tested. Besides, we have compared the antibacterial effect of 4MMP-GNC with other GNCs reported in the literature from 2017 against gram-positive bacteria (including MDR strains, **SI, Table S5**). Our 4MMP-GNC demonstrates a better antibacterial effect than >83% of other antibacterial GNCs in terms of their MICs. Moreover, in most other studies, the ligands used for GNC capping are inherently "active" and display antibacterial properties on their own. Moreover, all the previous literature does not involve the regulation of the GNC conformation. In contrast, herein we have demonstrated that, by changing the ligand feed ratio, we have not only activated neutral non-antibacterial ligands but also controlled the conformation of atomically precise GNCs to turn them into highly potent antibacterial agents, which has fundamentally different mechanisms from most other antibacterial GNCs reported in the literature.

Table 4. MICs of the MRSA strain in this study against different antibiotics

Ery[a)]	Azi	Kan	Tet	Van	Dap
4	32	>256	64	1	0.5
Ofx	Lvx	Cln	Tob	Chl	
128	64	64	256	8	

[a)]Ery, erythromycin; Azi, azithromycin; Kan, kanamycin; Tet, tetracycline; Van, vancomycin; Dap, daptomycin (with 1.25 mM Ca^{2+}); Ofx, ofloxacin; Lvx, levofloxacin; Cln, clindamycin; Tob, tobramycin; and Chl, chloramphenicol
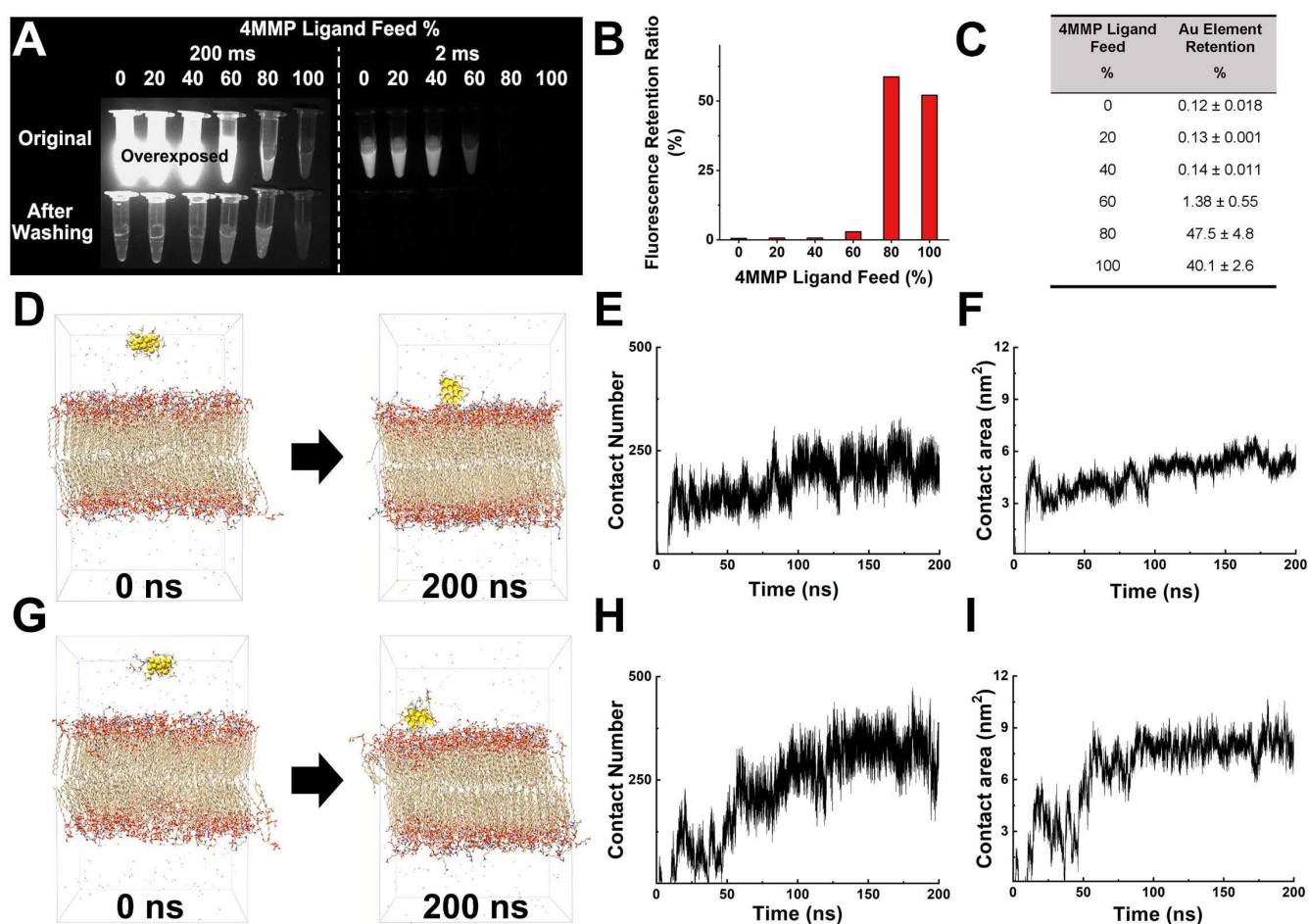
18

Figure 3. Study the effect of the 4MMP feed ratio on the binding of 4MMP-GNC to MRSA to explain the relationship between the 4MMP feed ratio and the antibacterial effect of 4MMP-GNC. (A) NIR fluorescence of mixtures of GNCs (with different 4MMP feed ratios) and equal amounts of MRSA for each group before (top) and after washing (bottom). Exposure times were set at both 2 and 200 ms to display the results of each group in one graph. (B) Statistics of the fluorescence retention rate on MRSA after washing to remove unbound GNCs. (C) ICP–MS analysis to prove the binding rate of GNCs with different 4MMP feed ratios to MRSA. GNCs prepared with 80% 4MMP ligand feed have a higher binding affinity for MRSA than other GNC species. (D) Molecular dynamic simulation of $Au_{23}(4MMP)_{16}$ (corresponding to 100% 4MMP

feed) before and after binding to MRSA cell membrane. (E) Statistics of contacts and (F) contact area of $Au_{23}(4MMP)_{16}$ binding with MRSA cell membrane during 10 ns interactions in steady state. (G) Molecular simulation of $Au_{23}(4MMP)_{14}(C5)_2$ (corresponding to 90% 4MMP feed) before and after binding to MRSA cell membrane. (H) Statistics of contacts and (I) contact area of $Au_{23}(4MMP)_{14}(C5)_2$ binding with MRSA cell membrane during 10 ns interactions in steady state.

To explain why GNC with different 4MMP ligand feeds have different antibacterial effects, we aliquoted the MRSA solution and incubated with the same amount of GNCs with different 4MMP feed ratios for 6 h, recorded the NIR fluorescence in each group, eluted unbound GNCs and then remeasured the NIR fluorescence intensity of MRSA under the same volume in each group to determine their binding capacity (**Figures 3A and 3B**). Despite exhibiting strong fluorescence, GNCs prepared with 0–60% 4MMP feeds all gave very low fluorescence retention (<3%), indicating little binding or entry into MRSA. In contrast, the GNC prepared with 80% 4MMP feed showed the highest fluorescence retention (~59%) in MRSA, indicating that it has the highest affinity (and thus a high antibacterial effect) for MRSA. To exclude other factors affecting the fluorescence signals, we digested the MRSA cells and measured the Au contents bound to MRSA with inductively coupled plasma mass spectrometry (ICP–MS). The ICP–MS results agreed well with the NIR fluorescence results above, where the 80% 4MMP-fed group demonstrated higher Au retention (~47%) than all other species, indicating its higher MRSA binding affinity and/or penetration than all other groups (**Figure 3C**). To further explain why 4MMP-GNC has better antibacterial potency than that prepared with 100% 4MMP feed, which is also Au_{23} NC, we performed a molecular simulation study on the interactions between the GNCs and MRSA cell membrane. We used a 7:3 ratio of 1,2-dipalmitoyl-sn-phosphatidylglycerol to 1,2-dipalmitoyl-sn-3-aza-

20

dehydroxylysyl-phosphatidylglycerol to mimic the composition of bacterial cell membranes[62]. Both $Au_{23}(4MMP)_{16}$ and $Au_{23}(4MMP)_{14}(C5)_2$ NCs (corresponding to GNCs prepared with 100% and 90% 4MMP feeds, respectively) were modeled for their interactions with the stabilized simulated cell membrane (**Figures 3D** and **3G**). On average, each $Au_{23}(4MMP)_{16}$ had 1 hydrogen bonding site and 211 hydrogen bond contacts with the MRSA cell membrane within 10 ns of stable interactions (**Figure 3E**), with an average contact area and binding energy of 5.38 ± 0.30 nm^2 and 446.3 ± 86.2 kJ mol^{-1}, respectively. The observed positive binding energy indicates that the interaction is predominantly driven by entropy, likely attributable to hydrophobic interactions. (**Figure 3F**). In contrast, the average number of hydrogen bonding sites and the overall number of interactions within 10 ns for $Au_{23}(4MMP)_{14}(C5)_2$ were 3 and 295, respectively, both of which were higher than those in $Au_{23}(4MMP)_{16}$ (**Figure 3G**). Besides, the contact area and binding energy in $Au_{23}(4MMP)_{14}(C5)_2$ were increased to 8.02 ± 0.70 nm^2 and -105.5 ± 40.6 kJ mol^{-1}, respectively. Its contact area was considerably larger than that in $Au_{23}(4MMP)_{16}$, and moreover, the interaction was changed into enthalpy-driven (**Figures 3H** and **3I**). Thus, although the C5 ligand does not possess an antibacterial effect, replacing two 4MMP ligands with two C5 ligands on the Au_{23} NC significantly enhanced the binding of 4MMP-GNCs with MRSA cell membranes, giving rise to a markedly stronger antibacterial effect over the pure 4MMP ligand counterpart. These results suggest that the ratio of both thiol ligands on the GNC surface determines their binding to MRSA and hence their antibacterial properties.

To probe the antibacterial mechanism of 4MMP-GNC, we first constructed the time-dependent bactericidal curve of 4MMP-GNC alongside antibiotics of different antibacterial mechanisms. Since Van is a glycopeptide that inhibits bacterial cell wall synthesis, treatment with Van at MIC levels induces bacterial cell membrane rupture

and reduces MRSA counts (**Figure 4A**). Indeed, the number of MRSA colonies treated with Van (1× MIC, 1 µg mL^{-1}) was reduced by ~75% within the first 2 h and by 93.4% at the end of the experiment (12 h). In contrast, the bactericidal effect of Dap (1× MIC, 0.5 µg mL^{-1} with 1.25 mM Ca^{2+}) was initially slow, and the MRSA colonies were reduced by only ~26% in the first 2 h. Subsequently, its reduction rate accelerated, and by 4 h, the MRSA number was reduced by 96.3%, demonstrating a completely different killing pattern from Van. Although the bacterial number recovered after that, indicating the incomplete elimination of MRSA cells, possibly due to resistance development. Notably, the antibacterial activity of 4MMP-GNC at a concentration of 1× MIC (2 µg mL^{-1}) exhibited a gradual yet sustained pattern, which is distinct from the effects observed with Van and Dap[63]. In the first 2 h, its bactericidal curve resembled that of Dap, although no rapid decrease in the bacterial number was observed at 4 h, a sharp contrast to that of Dap. Instead, the bacterial number showed a constant decrease (by ~90%) and reached only ~0.1% of that of phosphate-buffered saline (PBS) control at 12 h. This effect of slowly inactivating bacteria observed in 4MMP-GNC differs significantly from those of common antibiotics.

We further recorded the cell morphologies of the untreated and 4MMP-GNC-treated MRSA cells by scanning electron microscopy (SEM) (**Figure 4B**). We did not observe any significant morphological deformation of the MRSA cells, except for slight shrinkage and withering of the bacteria compared with the plump shape of the PBS control. These findings suggest that the reduction in MRSA cell viability following treatment with 4MMP-GNC is not attributable to cell membrane disruption. In addition, TEM images indicated no evident changes in the shape or structure of treated MRSA cells. No cell content leakage or membrane rupture was observed. However, the zoom-

in has displayed some blebbing of the cell membrane in cells after 4MMP-GNC treatment (**Figure 4C**).

We further examined 4MMP-GNC distribution by measuring the Au contents on the MRSA cell membrane and within cells by TEM energy-dispersive spectroscopy. We found a wide co-distribution of Au with O, mainly on the MRSA cell envelope and within MRSA cells, indicating the extensive contact of 4MMP-GNCs with MRSA and the occurrence of entry (**Figure 4D**). An area scan of the element distribution demonstrated higher Au content on the cell membrane than within cells, indicating that 4MMP-GNCs first bind to the MRSA membrane before entry into cells (**Figures 4E** and **4F**).
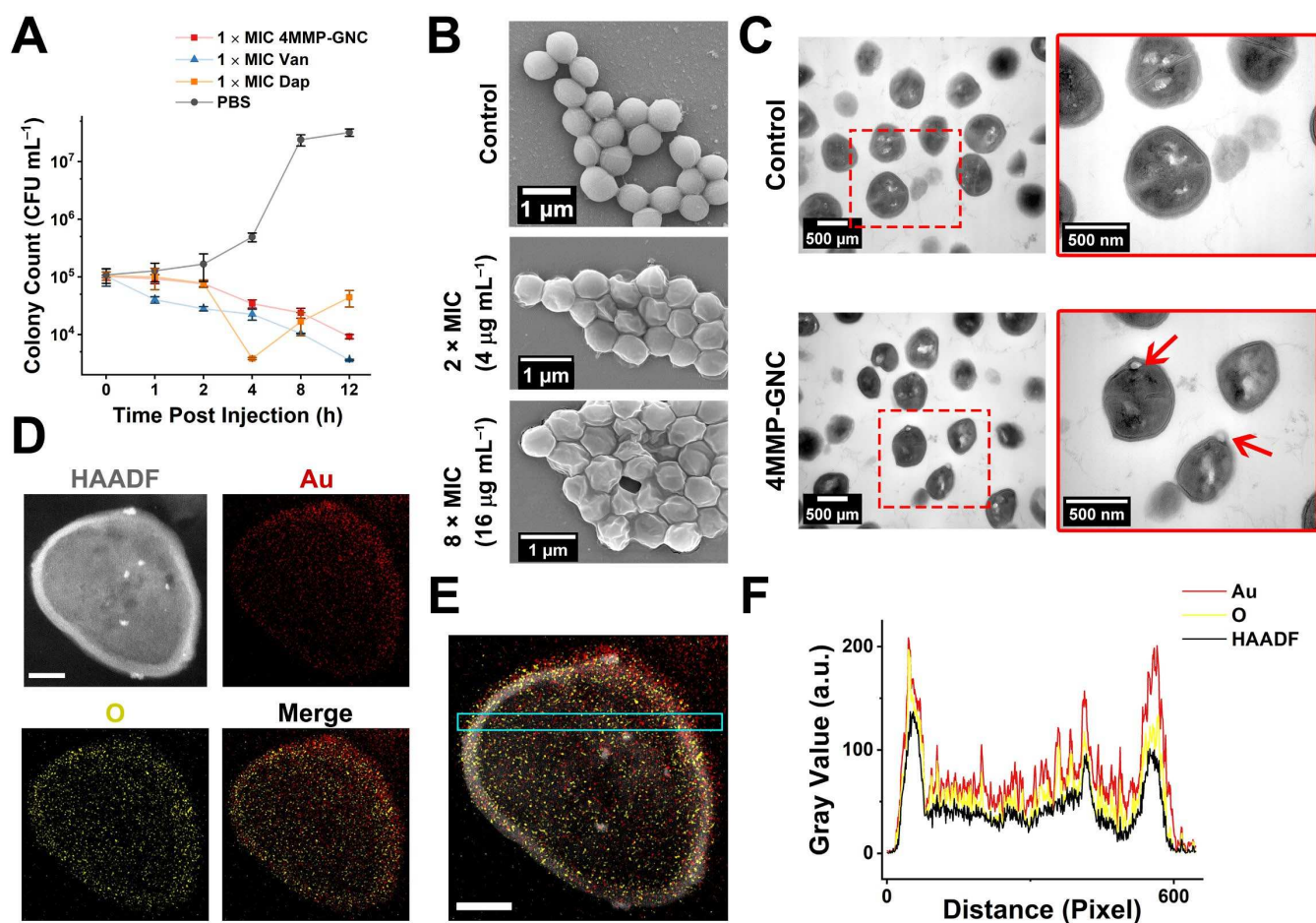
Figure 4. Characterization of the antibacterial properties of 4MMP-GNC. (A) The time–bactericidal curves of antibiotics and 4MMP-GNC against MRSA under 1× MIC dose. (B) SEM images of MRSA cells after treatment with PBS (negative control) and 4 (2× MIC) or 16 µg mL^{-1} (8× MIC) 4MMP-GNC. (C) TEM images and the zoom-in of MRSA cells after treatments of PBS (negative control) or 16 µg mL^{-1} (8× MIC) 4MMP-GNC. Blebbing on the cell envelope is indicated by red arrows. (D) TEM image and energy-dispersive spectroscopy mapping images of Au, O element and the merged image of the ultrathin section of MRSA cells treated with 4MMP-GNC (scale bar: 100 nm). (E) Selected scan area of the energy-dispersive spectrometer image (indicated by a cyan box) and (F) corresponding element distribution statistics on the sections of MRSA treated with 4MMP-GNC (scale bar: 100 nm).

The results above suggest that 4MMP-GNC interacts with the MRSA cell membranes, but the interaction does not affect the cell membrane integrity nor cause leakage of the cell contents while still being able to induce cell death. Compared to many antimicrobial agents that induce the rupture of bacterial cells by either directly inhibiting bacterial cell wall synthesis (e.g., Van or penicillins) or damaging the membrane integrity (e.g., antimicrobial peptides), the antibacterial action of 4MMP-GNC is relatively mild and uniquely nondestructive. Several new antibiotics, including Dap, kill bacteria in such non-lytic ways[64], thereby avoiding the extensive leakage of bacterial endotoxins, which can reduce the overreaction of the host immune system or excessive physiological damage. This could serve as a relatively safe approach for controlling pathogens. Considering the close similarity in the initial bactericidal curve between 4MMP-GNC and Dap, we speculated that their antibacterial mechanisms might be similar. Thus, we further investigated its antibacterial mechanisms alongside Dap for a detailed comparison.

24

Daptomycin, a cyclic lipopeptide antibiotic, is utilized for the management of acute infections caused by gram-positive bacteria that are refractory to conventional antibiotic therapies, such as endocarditis and septicemia[65]. Although the antibacterial mechanism of Dap is not yet fully understood, it has been classified as a membrane-active antibiotic[66]. Similar to 4MMP-GNC, Dap does not elicit the complete rupture of the cell membrane that is typically observed with antimicrobial peptides or surfactants[67]. Thus, we performed several experiments to investigate how 4MMP-GNC treatment affects the normal physiological activities of MRSA.
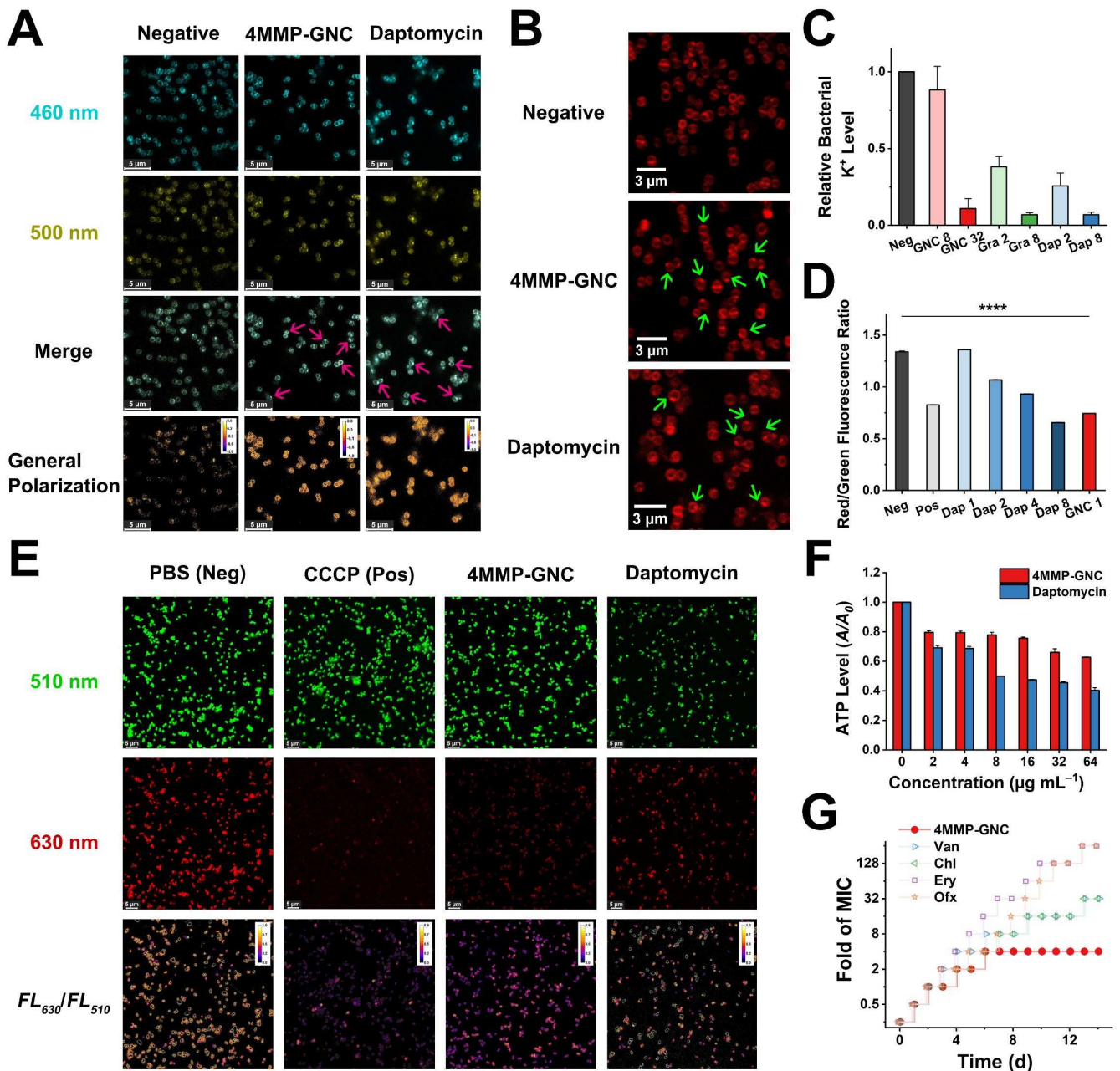
Figure 5. Studies on the antibacterial mechanisms of 4MMP-GNC. (A) Confocal fluorescence microscope images of laurdan fluorescence at 460 and 500 nm in MRSA cells treated with PBS, Dap, and 4MMP-GNC. Magenta arrows indicate the laurdan-clustered regions. (B) Membrane phospholipid liquefaction assay with DilC12(3). The membrane surface-aggregated domains of DilC12(3) are labeled with green arrows, indicating phospholipid liquefaction induced by 4MMP-GNC or Dap binding. (C) Comparison of K$^+$ levels among MRSA cells treated with different doses of 4MMP-

GNC, gramicidin (Gra), and Dap (Unit: $\mu g\ mL^{-1}$). (D) Statistical results and (E) fluorescence images of membrane potential comparison among MRSA cells treated with PBS (negative control), carbonyl cyanide 3-chlorophenylhydrazone (CCCP; positive control), Dap, and 4MMP-GNC, analyzed using the fluorescence ratio between 630 and 510 nm. (F) The ATP level of 4MMP-GNC- and Dap-treated MRSA cells at different doses. (G) Comparison of drug resistance development between 4MMP-GNC and traditional ophthalmic antibiotics.

The binding of Dap can affect the membrane fluidity and cause rigidification of the phospholipid bilayer[66] to suppress the normal physiological activities of bacteria. To evaluate whether 4MMP-GNC has similar effects on the MRSA cell membrane, we used a membrane fluidity-sensitive dye, laurdan, whose fluorescence is sensitive to the lipid head density (**Figure 5A**)[63]. The general polarization (GP) value of MRSA treated with Dap increased significantly over the PBS control, indicating the rigidification of the MRSA cell membrane. Similarly, treatment with 4MMP-GNC resulted in an increase in GP value and a decrease in membrane fluidity. This was accompanied by the formation of aggregated microdomains and condensed phospholipid regions on the MRSA cell membrane, which were also observed after Dap treatment. Thus, the formation of condensed microdomains and rigidification of bacterial cell membranes, induced by GNC–phospholipid interactions, are the most likely antibacterial mechanisms for 4MMP-GNC.

To further characterize the microdomains formed on MRSA cell membranes, a lipid fluidity-indicating dye, DilC12(3), was used to stain bacterial cells. We observed DilC12(3)-clustered regions in both Dap- and 4MMP-GNC-treated groups (**Figure 5B**), suggesting they both promote the aggregation of phospholipids in the fluid lipid domains and cause cell membrane rigidification. The perturbation of the organization

27

of the cell membrane affects a series of vital cellular processes based on the cell membrane, constituting the antibacterial mechanism of Dap for non-lytic bactericidal[63]. Due to the similarity of the membrane-active phenomenon in inducing cell membrane rigidification and phospholipid aggregation between 4MMP-GNC and Dap, it is likely that it also inactivates bacteria through a similar mechanism. It is worth mentioning that, compared to gram-positive bacterial cell membranes, mammalian cell membranes have unique cholesterol components, which have been proven to inhibit the binding of Dap[68]. Due to their similar mechanism, this could partially explain the selectivity of 4MMP-GNCs between somatic and bacterial cells as a basis for their high biocompatibility.

The antibacterial mechanism of many membrane-active antibiotics (e.g., Dap or Gramicidin A (Gra A)[63]) is strongly related to the efflux of certain metal ions due to membrane perturbation. To verify whether 4MMP-GNC can cause ion loss, we compared the levels of K^+ in MRSA cells following 4MMP-GNC treatment. Gra A and Dap were employed as positive controls. Our results demonstrate that, similar to both antibiotics, 4MMP-GNC also reduced the K^+ level in MRSA cells, thereby interfering with the normal membrane potential of bacteria (**Figure 5C**). Previous studies have confirmed that treatments with some peptide antibiotics, including Dap, can dissipate membrane potential in gram-positive bacteria. To determine whether 4MMP-GNC also induces this phenomenon, we used a membrane potential dye, DiSC3(5), whose fluorescence depends on the degree of depolarization of the bacterial cell membrane. Treatment with 4MMP-GNC resulted in a significantly greater increase in DiSC3(5) fluorescence compared to Dap at equivalent doses, suggesting that 4MMP-GNC is more effective in disrupting the membrane potential of MRSA cells (**SI, Figure S7**). The dissipation of membrane potential in MRSA cells was further quantified using a

MycoLight ratiometric fluorescent bacterial membrane potential kit in conjunction with laser scanning confocal microscopy. The red-to-green fluorescence ratio decreased with the increased membrane potential dissipation (**Figures 5D** and **5E**). Carbonyl cyanide 3-chlorophenylhydrazone, a protonophore that increases plasma membrane permeability to hydrogen ions and induces membrane potential dissipation, was employed as a positive control. Both 4MMP-GNC and Dap caused clear shifts in the overall FL_{630}/FL_{510} (red-to-green) fluorescence ratio from high to low, as corroborated by statistical analysis, confirming the dissipation of membrane potential following treatment with both Dap and 4MMP-GNC.

Despite such similarities in antibacterial mechanisms, marked differences in antimicrobial patterns between 4MMP-GNC and Dap were also identified (**Figure 4A**). A specific feature of Dap is that its antibacterial potency is strongly dependent on Ca^{2+} concentration (with 1.25 mM Ca^{2+} giving the best antibacterial effect). This is presumably because Dap is negatively charged; the presence of Ca^{2+} ions can effectively screen the electrostatic repulsion between negatively charged bacteria and Dap molecules[65]. In contrast, the antibacterial property of 4MMP-GNC was unaffected by Ca^{2+} content, indicating that 4MMP-GNC has robust stability and exerts a consistent antibacterial effect (**SI, Table S6**). The neutral charge of the C5 and 4MMP ligands on GNCs suggests that the presence of Ca^{2+} ions would not be expected to significantly alter their interactions with bacteria cell membranes and, consequently, the antibacterial capacity of 4MMP-GNC.

The levels of ATP and ATPase in MRSA cells were quantified following treatment with either 4MMP-GNC or Dap to verify their influences on MRSA energy metabolism further. Both treatments significantly reduced the ATP levels in MRSA in a dose-dependent manner (**Figure 5F**). As ATP is synthesized by ATP synthase anchored on

29

the MRSA cell membrane driven by the proton gradient (membrane potential), this enzyme activity should be sensitive to the membrane environment and potential. As shown in the previous section, the binding of 4MMP-GNC to cell membranes can cause phospholipid clustering, membrane liquefication, and membrane potential depolarization. All these could interfere with the ATP synthase activity, reducing the bacterial ATP level and metabolic activity. However, Dap treatment did not reduce the ATPase activity in MRSA. In contrast, 4MMP-GNC treatment significantly and dose-dependently reduced the ATPase activity in MRSA (**SI, Figure S8**). Thus, different from Dap, by affecting both ATP synthesis and consumption, 4MMP-GNC comprehensively interferes with the normal energy metabolic pathways of MRSA.

To elucidate the specific protein types impacted by GNC treatment, a proteomic analysis was conducted to compare MRSA cells treated with either PBS or 4MMP-GNC. A volcano plot analysis revealed that approximately 100 protein expressions were significantly altered following treatment with 4MMP-GNC. Of these, approximately 50% exhibited up-regulation, while the remaining 50% exhibited down-regulation (**SI, Figure S9**). Analysis of protein expression and classification of protein domain enrichment demonstrated that the treatment of 4MMP-GNC significantly affected ATPases, especially those associated with various cellular activities or the so-called AAA family (**SI, Figure S10**, labeled in red boxes)[69]. This result is highly consistent with the observations that 4MMP-GNC affects the ATPase function, as shown in **Figure S8** (SI). The AAA family enzymes (e.g., Clp ATPases) are strongly related to the virulence, resistance, growth, and survival of *S. aureus*[70] [71] [72]. Thus, the binding of 4MMP-GNC to the bacterial cell membrane and its subsequent entry to affect pathways related to the cell membrane represents a potential antimicrobial mechanism. A further gene ontology annotation statistics of differentially expressed

30

proteins indicated that 4MMP-GNC also affected a series of cellular metabolic activities and interrupted enzyme activities in MRSA. Most of these influences are highly related to cell parts, especially cell membranes (**SI, Figure S11**). Analysis of the gene ontology function enrichment chart revealed differential expression of several oxidoreductases and dehydrogenases involved in cellular respiration and metal ion metabolism. Most of these are membrane enzymes that play an important role in MRSA virulence, survival, and proliferation (**SI, Figure S12, labeled in red boxes**) [73] [74] [75]. These influences on the oxidoreductases' activity were also reported for other metallic nanomaterials[76] [77]. After entering cells, the downregulation of DNA topoisomerase expression (especially those depending on ATP hydrolysis) enables 4MMP-GNC to exhibit strong antibacterial effects against *S. aureus* (**SI, Figure S12, labeled in blue boxes**).

The antibacterial mechanisms of 4MMP-GNC can thus be summarized into five steps. 1) 4MMP-GNC effectively binds to the MRSA cell membrane and enters bacterial cells. 2) By attracting phospholipids, the binding of 4MMP-GNC causes membrane rigidification and liquefaction. 3) Through ion loss, 4MMP-GNC leads to membrane potential dissipation and disruption of normal bacterial physiological activities. 4) The disruption of membrane potential inhibits ATPase function, thereby affecting bacterial ATP levels and interfering with bacterial energy metabolism. 5) Through the influence of a series of enzymatic activities (related to cellular respiration and DNA replication), 4MMP-GNC can slowly but effectively inactivate MRSA without causing cell membrane rupture, thereby avoiding the overreaction of the host immune system.

Due to antibacterial GNCs normally having multiple antibacterial mechanisms, it is more difficult for bacteria to develop resistance against them than traditional antibiotics

31

that mostly exhibit a single antibacterial action[29] [78]. We tested the resistance development of an antibiotic-sensitive *S. aureus* strain over a 14-day period with four traditional ophthalmic antibiotics from different classes (Ery, Chl, Ofx, and Van, **Figure 5G**). Ery and Ofx cannot inhibit the development of drug resistance of *S. aureus*, and the antibiotic concentration required to inhibit bacterial growth rapidly increased to >64× MIC (original) within 10 days. For Van and Chl, although the development of drug resistance was slower than Ery and Ofx, it could still break through 8× MIC (original) within 10 days and continue to increase to 32× MIC (original) at the end of the experiment. In contrast, although some resistance towards 4MMP-GNC was observed at the initial sub-inhibitory concentration stage, it did not break through 4× MIC (original) or proliferate after repeated inoculations. This concentration only corresponded to 2× MBC (original), demonstrating that 4MMP-GNC is more effective in preventing *S. aureus* resistance development than conventional ophthalmic antibiotics.

In addition to the hemolytic results presented in **Figures 2C** and **S6**, the biosafety and biocompatibility of 4MMP-GNC to ocular cells were assessed using a human retinal epithelial cell line, ARPE-19. After 12 and 24-h incubation, the cell viability was analyzed using a cell live-dead staining kit as well as the 3-(4,5-dimethyl-2-thiazolyl)-2,5-diphenyltetrazolium bromide-based cell proliferation assay[79]. Compared with the PBS control, the viability of ARPE-19 cells showed little change even under a high dose of 4MMP-GNC treatment (40× MIC against MRSA). In addition, cell staining with propidium iodide (PI) and Calcein-AM for dead and live cells, respectively, revealed no obvious changes in live cell morphology or number from the PBS control, confirming no significant cytotoxicity and excellent biocompatibility of 4MMP-GNC (**Figure 6A** and **Figure 6B**). In addition, Following 12 and 24-hour incubations with

32

high doses of 4MMP-GNC (60× MIC against MRSA), human umbilical vein endothelial cells (HUVECs) exhibited high viability and no significant differences in the proportion of dead cells compared to the PBS control (**Figure 6C** and **SI, Figure S13**). Together these results demonstrate the high biocompatibility and extremely low cytotoxicity of 4MMP-GNC against endothelial and retinal epithelial cells.
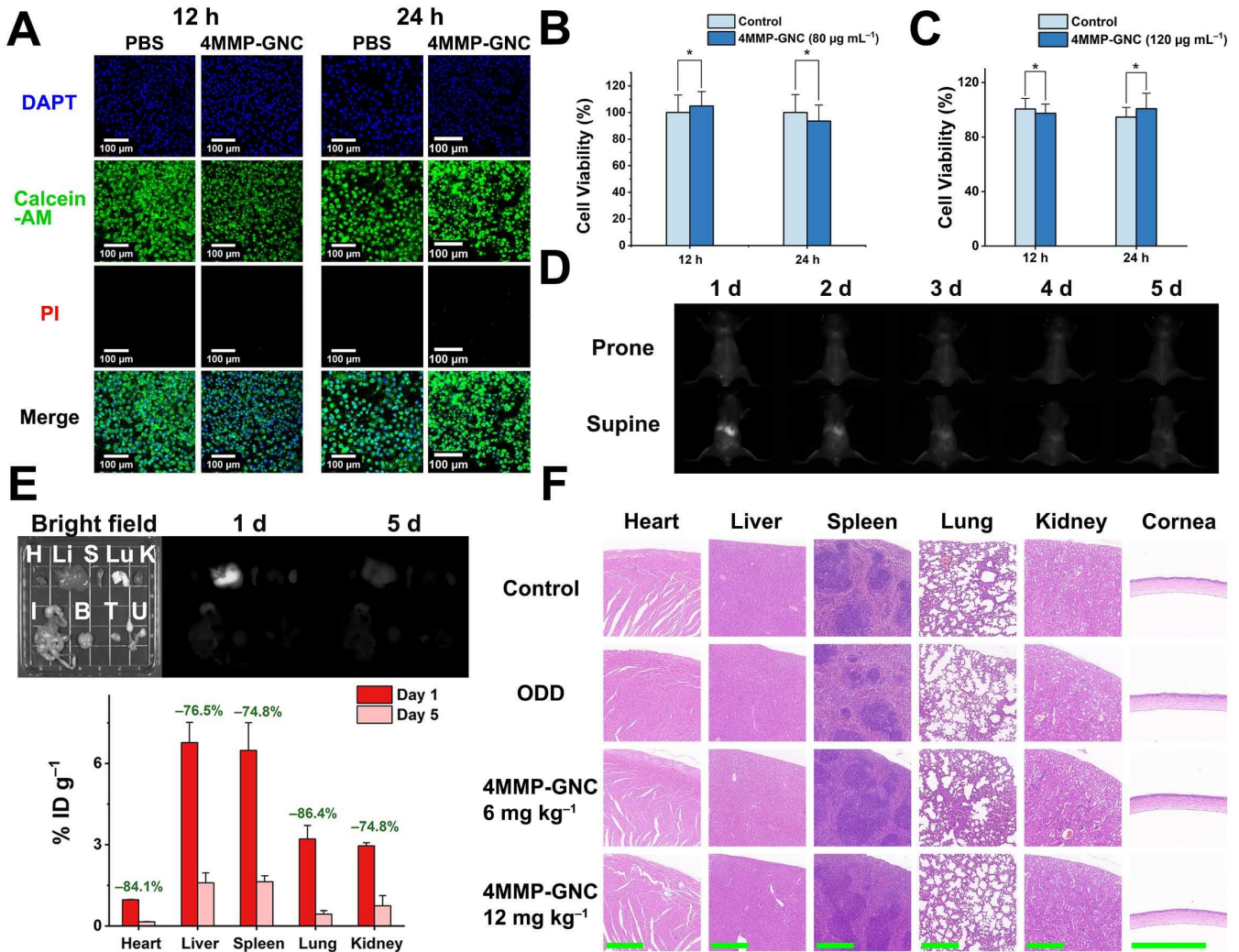

Figure 6. Biocompatibility and metabolism analysis of 4MMP-GNC at the cellular, tissue, and organismal levels. (A) The live–dead cell staining results of the ARPE-19 cell line after 12 or 24 h of incubation with 80 µg mL^{-1} (40× MIC) 4MMP-GNC. No increase in the number of dead cells (indicated by PI fluorescence) was observed in the 4MMP-GNC group compared with that in the PBS control. Viability of (B) ARPE-19

cells and (C) HUVECs after 12 and 24 h of incubation with 80 µg mL^{-1} (40× MIC) and 120 µg mL^{-1} (60× MIC) 4MMP-GNC respectively, as measured using the MTT assay (*: P >0.05). (D) Daily NIR fluorescent photographs of mice after intravenous injection of 6 mg kg^{-1} 4MMP-GNC (λ_{EX} = 808 nm, 32 mW cm^{-2}, 400 ms). (E) Upper: organ distribution of mice after intravenous injection of 6 mg kg^{-1} 4MMP-GNC (λ_{EX} = 808 nm, 32 mW cm^{-2}, 300 ms; H—heart, Li—liver, S—spleen, Lu—lung, K—kidney, I—gastrointestinal tract, B—brain, T—thymus, and U—uterus); lower: ICP-MS analysis of Au element differences in each major organ on the first day and the fifth day (n = 4). (F) Hematoxylin and eosin (H&E) staining results of the main organs (I.V.) and cornea (ODD: ocular drug delivery) after treatment with 4MMP-GNC via different administration methods. Compared with the PBS control, no obvious lesion or immune response was observed in 4MMP-GNC-treated cells, indicating the high biosafety of 4MMP-GNC (scale bar: 400 µm).

The *in vivo* biocompatibility of 4MMP-GNC was demonstrated through the analysis of blood routine as well as liver and kidney biochemical indices following ocular drug delivery or intravenous injection into the mouse tail vein. Compared to a PBS control, the intravenous application of 6 or 12 mg kg^{-1} (or 120 µg mL^{-1} 4MMP-GNC ocular administration at 6-h intervals) had no significant influence on blood cell count or liver and kidney indices. All these indicators were within the normal range, indicating negligible toxicity of 4MMP-GNC on the physiological activities of mice (**SI, Figure S14**). To study their organ distribution and metabolic process, we injected 6 mg kg^{-1} 4MMP-GNC into the tail vein of mice and monitored the GNC NIR fluorescence to characterize its organ distribution (**Figure 6D**). After 24 h, bright NIR fluorescence appeared in the abdomen of the mouse and mainly appeared in the liver, spleen, and

kidney, according to the anatomical observation (**Figure 6E**, upper). The fluorescence in the abdomen of the mice was significantly attenuated with the extension of time. Anatomical imaging of major organs was performed on the fifth day, and the fluorescence of the liver, spleen, and kidney was markedly reduced. We further analyzed Au content in each organ using ICP-MS. On day 1, the accumulation of GNCs was high in both the liver and spleen (both >7% ID g^{-1}). However, on the fifth day, the Au contents were decreased to <2% ID g^{-1}, indicating a reduction of >74%, proving that 4MMP-GNC has a reasonable metabolic rate and can effectively excrete from organs (**Figure 6E**, lower). These results are consistent with the high *in vivo* biosafety of 4MMP-GNC observed. We also compared the H&E-stained sections of major organs and found no observable pathological changes after the intravenous administration of 12 mg kg^{-1} 4MMP-GNC compared to the negative control (**Figure 6F**). The results further confirmed the high *in vivo* biosafety of 4MMP-GNC.

In addition, to verify the effect of long-term ocular administration as an eye drop on the health of mice, we extended the ocular administration period to 21 days and then remeasured the level of blood routines as well as liver and kidney blood biochemical indicators (**SI, Figure S15A–F**). Compared with the PBS control, long-term ocular administration did not affect these indicators, and the pathological sections of various organs all showed healthy structures (**SI, Figure S15G**). At the administration site, the cornea, which was in direct contact with 4MMP-GNC, showed no thickening or abnormality. Photographs of the eye also do not have any visible lesions. All these results prove the excellent safety of 4MMP-GNC for long-term ocular use. To characterize the effect of high 4MMP-GNC concentrations on mouse health, we intravenously administered 110 mg kg^{-1} 4MMP-GNC (55× MIC against MRSA) in mice and monitored their body weight. This systemic application of such a high dose

35

did not cause mortality in any mouse. The body weight of the treated group was comparable to that in the PBS control group for 7 days following GNC administration, suggesting no significant damage to vital organs (**SI, Figure S16**). These experiments demonstrate that no measurable side effects or toxic accumulation are produced, even under a high-dose (110 mg kg^{-1}) or a long-term (21-day) application, confirming that 4MMP-GNC has high biological safety at the cellular, tissue, and *in vivo* mouse model levels.

In addition to biosafety, stability is also a key factor affecting the application of nanomaterials. We compared the UV−vis spectra of 4MMP-GNC before and after storage at room temperature, sealed in darkness for 3 months. There was only a slight decrease in the absorption peak, with the shape of the curve remaining the same, proving that the GNC structure has not changed significantly after long-term storage (**SI, Figure S17**). Moreover, the scalability of 4MMP-GNC production was also demonstrated by increasing the preparation volume 20-fold to 100 mL. Both the original and large-scale prepared 4MMP-GNC completely inhibited the growth of MRSA at 2 μg mL^{-1}, confirming no change in the antibacterial potency after scale-up preparation (**SI, Figure S18**).

Vancomycin, an antibiotic of last resort to control acute gram-positive bacterial infections, is regarded as the gold standard in treating MRSA infections, including keratitis[80]. Thus, we applied Van as a positive control to evaluate the practical antikeratitis effect of 4MMP-GNC. An *in vitro* keratitis model was established by excising the cornea from a porcine eye containing a scleral ring. Subsequently, a circular wound with a diameter of 8 mm was created within the stromal layer of the porcine cornea. The dome of the cornea was disinfected and then filled with LB agar as the culture medium to maintain the normal physiological shape of the eyeball and

36

simulate the anterior chamber and vitreous structure[81]. Then, 1 µL of 1×10^4 CFU mL^{-1} MRSA cells were inoculated onto the wound to mimic keratitis. After a 12-h incubation, the wound was treated with PBS as a negative control, Van (32 µg mL^{-1}, 32× MIC) as a positive control, or 32 µg mL^{-1} (16× MIC) 4MMP-GNC. The treatment regimen consisted of thrice-daily administration at 6-h intervals. At the end of the treatment, the porcine cornea was photographed, and then the infected wound was separated for plate coating to count the MRSA colonies. Among the three groups, keratitis was most severe in the PBS-negative control group, where MRSA colonies were widely connected to form a thick biofilm (**Figure 7A**). In addition, the colony spread to the edge of the scleral tissue through gullies and formed a ring on the bottom agar plate, indicating the high viability and proliferation of MRSA. Meanwhile, the Van-treated cornea had reduced biofilm formation in the center of the wound area and less diffusion to the periphery. The bacterial ring was also thinner. However, even Van at 32× MIC did not effectively inhibit the growth of MRSA, likely due to the development of resistance. In contrast, only separate colonies were formed in the 16× MIC GNC-treated group, and biofilm was barely visible, with no observable spread of MRSA colonies to the bottom agar plate. The plate coating also revealed similar results. Compared with the PBS control group, the Van-treated group had a significantly lower number of colonies. However, the GNC-treated group showed the lowest number of MRSA colonies, proving that in the *in vitro* keratitis model, 4MMP-GNC can achieve an even better therapeutic effect than Van at a lower MIC multiple (**Figure 7B**).

At the end of the experiment, the corneas were separated, fixed, sectioned, and then subjected to H&E and Gram staining (**Figure 7C**). In the PBS (negative control) group, distinct and condensed purple spots were observed at the site of infection. Further analysis using Gram staining confirmed the presence of gram-positive bacteria,

37

specifically MRSA. The Van-treated group showed significantly reduced staining of MRSA cells, while the GNC-treated group showed the least staining. These results agreed well with those of bacterial counting, confirming the high efficacy of 4MMP-GNC in treating MRSA infection in the *in vitro* keratitis model.
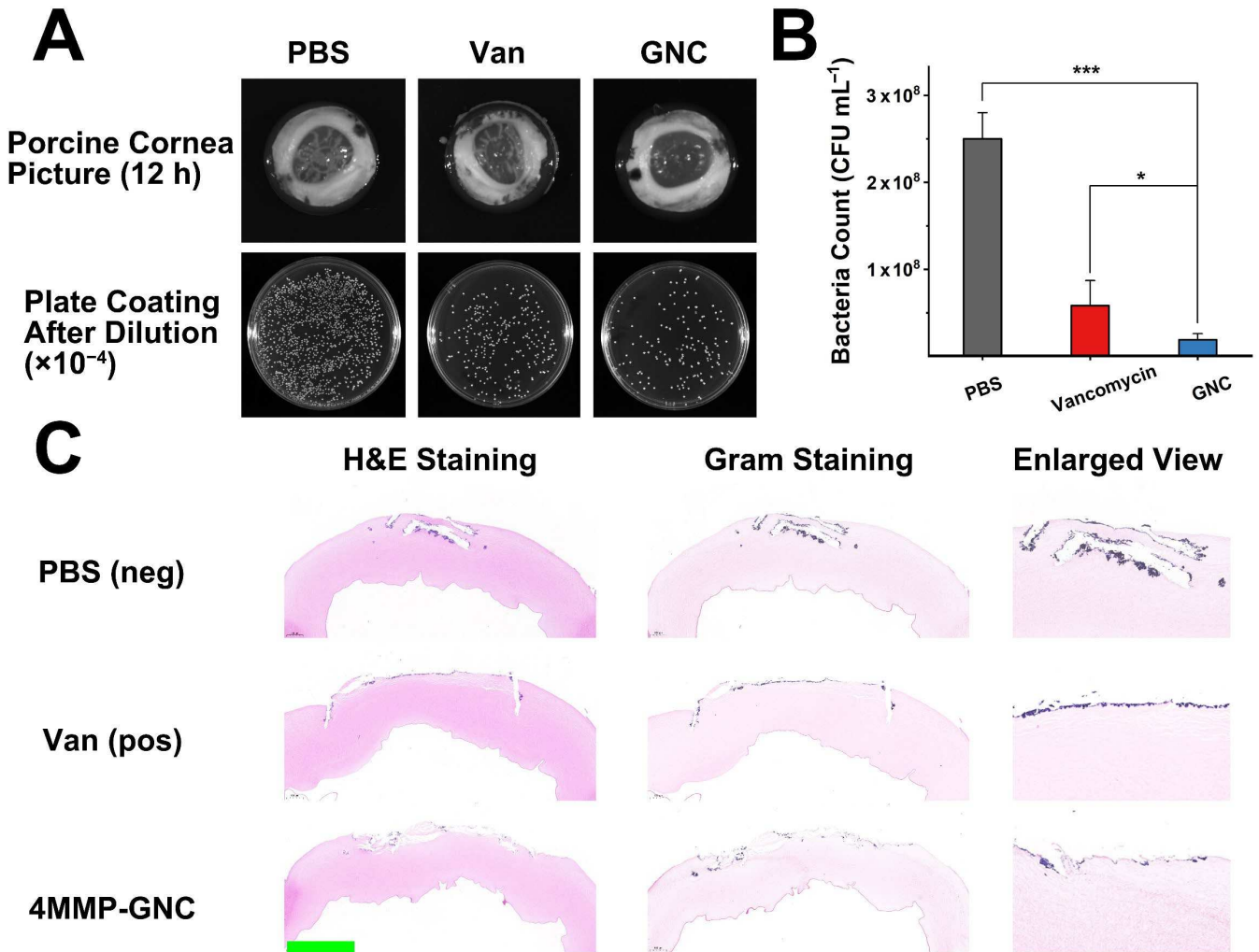

Figure 7. The therapeutic effects of 4MMP-GNC on the *in vitro* keratitis model were compared to that of Van, an antibiotic of last resort. (A) Optical images of porcine corneas treated with PBS (negative control), Van (positive control), and 4MMP-GNC (upper), as well as the diluted bacterial plating results of each group under ambient light (lower). (B) Statistical results of bacterial plate coating of MRSA-infected porcine corneas after different treatments (*: $P > 0.05$, ***: $P < 0.01$). (C) H&E and Gram staining

results of the porcine corneas in different groups. On the right, the Gram staining signal of the gram-positive infection area is further enlarged. A clear positive purple signal was observed in the PBS control. The positive staining signals were greatly reduced in the Van- and 4MMP-GNC-treated groups (scale bar: 2 mm).

We then administered 4MMP-GNCs to an *in vivo* murine keratitis model. This model was established by anesthetizing mice and creating a series of perpendicular scratches deep in the stroma on the unilateral cornea of mice with a syringe needle (**Figure 8A–D**)[82]. The wound was then infected with 2 μL of MRSA bacterial solution (5×10^8 CFU mL^{-1}) for 24 h, followed by treatment with PBS (negative control), Van (positive control), or two different doses of 4MMP-GNC thrice daily at 6-h intervals for 3 consecutive days. The infection was monitored and photographed at the start of daily experiments, and the area of eye ulceration was measured. We also collected a swab of the eye discharge for colony counting daily. We compared the area of opacity induced by ulceration on the cornea and found that in contrast to the severe eye ulceration and increased eye discharge observed in the PBS control, treatment with 32× MIC (32 μg mL^{-1}) Van reduced the extent of opacity and showed a tendency to cure the ulceration. However, on day 3, the scratches on the cornea were still visible, accompanied by signs of inflammation (e.g., swelling and angiogenesis). Similarly, treatment with 8× MIC (16 μg mL^{-1}) 4MMP-GNC showed similar effects to that with Van, where the opacity was generally cured by day 3, although full recovery of the mouse corneal wound was not achieved. In contrast, treatment with 32× MIC (64 μg mL^{-1}) 4MMP-GNC not only significantly reduced the infection induced by MRSA but also accelerated the corneal wound healing.

The bacterial colony counts from the swabs of the eye discharges were completely consistent with this trend, with the PBS group showing the highest MRSA load (**Figure**

39

8C), while the 32× MIC of Van- and 8× MIC (16 µg mL^{-1}) GNC- treated groups showed similar tendencies with a moderate decrease in bacterial counts. Meanwhile, the 32× MIC (64 µg mL^{-1}) GNC-treated group showed the most rapid reduction and lowest final count of MRSA, at approximately 100-fold lower than the initial bacterial count. This result was distinctly different from that of the PBS group, indicating good control of MRSA infection. On day 3, the corneas were fixed and subjected to H&E and Gram staining (**Figure 8E**). The PBS-treated group demonstrated a thick and bumpy corneal surface. A closer examination revealed abundant purple-stained regions in the swollen area, indicating severe MRSA infection. In contrast, treatment with Van resulted in a significant reduction in the severity of infection. However, corneal thickness remained abnormal, potentially due to the presence of foci observed in ocular photographs. In addition, the corneal epithelial cells were disordered, indicating that full recovery of the wounds had not occurred. The low-dose GNC group showed similar findings to the Van group. However, the high-dose GNC group showed significantly reduced corneal thickness and well-stratified corneal epithelial cells, indicating a full recovery of the corneal wound.

To characterize the restoration of vision in mice, we used a small-animal optomotor response (OMR) analysis instrument to characterize and compare their eye movement responses. OMR is an innate orienting behavior elicited by full-field visual movement[83]. Compared with the PBS control group, the ability of treated mice to follow stripe movement progressively enhanced with the healing of ocular ulceration, indicating increased visual discrimination ability. Behavioral analysis software was utilized to acquire data pertaining to the direction and velocity of head movements. This information was subsequently used to compute the OMR index and generate a corresponding heat map. In both clockwise and anticlockwise stripe movements, the

40

4MMP-GNC-treated group showed an OMR index similar to that of the uninfected group, which was significantly higher than that of other treatment groups. This demonstrated the superiority of 4MMP-GNC in treating eye ulcerations and restoring vision in animals (**Figure 8F**). Thus, compared with Van, a gold standard for the clinical treatment of bacterial keratitis caused by MRSA, the fold of MIC for 4MMP-GNC is significantly lower than that of Van to produce the same therapeutic effect. In addition, at the same fold of MIC, 4MMP-GNC achieves a better therapeutic effect than Van, thus confirming the excellent therapeutic effect of 4MMP-GNC as a next-generation nanomedicine for treating MRSA-induced keratitis in the form of eye drops.
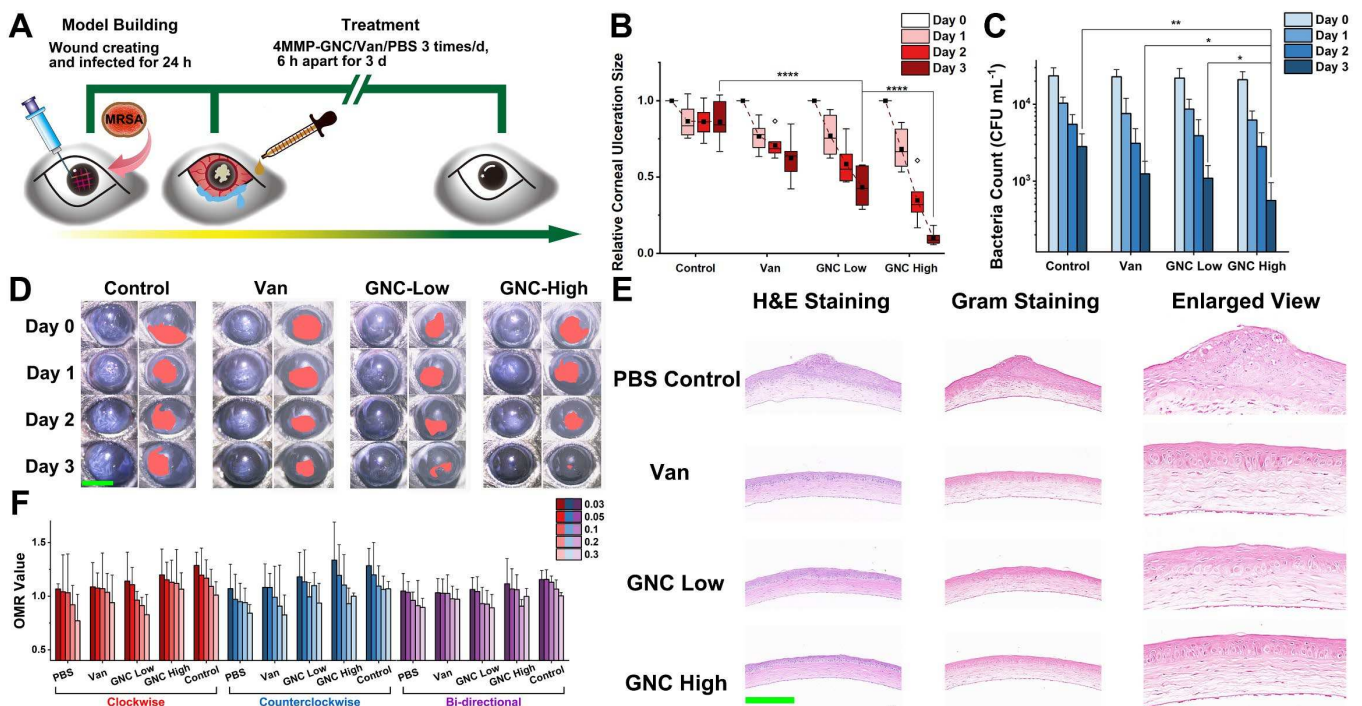
Figure 8. Antikeratitis effect of 4MMP-GNC in the *in vivo* murine keratitis model. (A) Flowchart of the *in vivo* experiment: mice were infected with MRSA for 24 h and then treated with PBS (negative control), 4MMP-GNC (16 and 64 µg mL^{-1}, corresponding to 8× MIC and 32× MIC, respectively), and Van (32 µg mL^{-1}, 32× MIC) for 3 days. At the end of the treatment, mice were sacrificed, and their corneal tissues were separated

and fixed for H&E and Gram staining. (B) Statistical results of the corneal ulcer size in different treatment groups. On day 3, ulcer sizes in the 64 µg mL^{-1} (32× MIC) 4MMP-GNC-treated groups were significantly smaller than the Van group, indicating that 4MMP-GNC was significantly more effective in treating MRSA-induced keratitis than Van. (C) Bacterial counting results of swabs from eye secretions in each group. Bacterial colony counts in 4MMP-GNC- and Van-treated groups did not differ significantly, but their differences from the PBS control group were significant. (D) Stereomicroscopy images of the status of eye infection in different groups. Ulcer size was greatly reduced in the 64 µg mL^{-1} (32× MIC) 4MMP-GNC-treated group, whereas that in the negative control groups showed little change. Additionally, the curative statuses associated with 16 µg mL^{-1} (8× MIC) 4MMP-GNC and 32 µg mL^{-1} Van (32× MIC) were similar (scale bar: 200 µm). (E) H&E and Gram staining results of the corneal sections in different groups. Except for the PBS control group, all other groups completely recovered from corneal injury, with the 64 µg mL^{-1} (32× MIC) 4MMP-GNC-treated group showing a smooth surface, as indicated in the scaled inset (scale bar: 2 mm) (*: $P > 0.05$; **: $0.01 < P < 0.05$; ****: $P < 0.001$; n = 5). (F) Bar chart of clockwise/counterclockwise/bidirectional OMR indexes of mice in each group under different spatial frequencies (0.03/0.05/0.1/0.2/0.3 cyc deg^{-1}). After MRSA infection, mice treated with PBS demonstrated a significant decrease in visual acuity, followed by those treated with 32 µg mL^{-1} (32× MIC) Van and 16 µg mL^{-1} (8× MIC) 4MMP-GNC. The mean visual acuity of the 64 µg mL^{-1} (32× MIC) 4MMP-GNC-treated group was greatly improved to the same level as that of the uninfected healthy control (n = 5).

3. Conclusion

In conclusion, our research has culminated in the development of a potent antimicrobial dual-ligand GNC, which has demonstrated efficacy in the treatment of

MRSA-induced keratitis. By controlling the feed ratios of two ligands (4MMP and C5) with different steric hindrances during GNC synthesis, the conformation of the GNC can be subtly adjusted from $Au_{25}(SR)_{18}$ to $Au_{23}(SR)_{16}$. Notably, the Au_{23} NC prepared with a 90% 4MMP feed (4MMP-GNC) exhibited greater potency than its mono-ligand counterparts, with a MIC of 2 $\mu g\ mL^{-1}$ against MRSA, comparable to many last-resort antibiotics. This result represents a significant (>1024-fold) enhancement in antibacterial potency over the corresponding pure ligands. This antibacterial difference was determined by the ratio of the two thiol ligands on the GNCs surface, and the change of only two molecules in capping altered their binding strength with the MRSA cell membrane significantly, resulting in different antibacterial effects. Surprisingly, treatment with 4MMP-GNC did not result in bacterial rupture; rather, it induced membrane rigidification and interfered with the energy metabolism to kill MRSA slowly but effectively. Due to its multiple antibacterial mechanisms, 4MMP-GNC outperformed conventional ophthalmic antibiotics in overcoming the rapid development of drug resistance. Moreover, 4MMP-GNC possesses long-term biological safety and stability, which ensures its broad application prospects. In both *in vitro* porcine corneal infection and *in vivo* murine keratitis models, treatment with 4MMP-GNC significantly inhibited bacterial colony formation, reduced bacterial load, and accelerated recovery from corneal ulceration. Thus, by controlling the ratios of two ligands with different steric hindrances, we have successfully synthesized 4MMP-GNC as an effective and flexible treatment for MRSA-induced keratitis in the form of eye drops.

4. Acknowledgment

5. Conflict of Interest

The authors declare no conflict of interest.

References

[1]   L. J. Luo, T. Y. Lin, C. H. Yao, P. Y. Kuo, M. Matsusaki, S. G. Harroun, C. C. Huang, J. Y. Lai, *J. Colloid Interf. Sci.* **2019**, *536*, 112.

[2]   L. Ung, P. J. M. Bispo, S. S. Shanbhag, M. S. Gilmore, J. Chodosh, *Surv. Ophthalmol.* **2018**, *64*, 255.

[3]   S. Tuft, T. F. Somerville, J. P. O. Li, T. Neal, S. De, M. J. Horsburgh, J. L. Fothergill, D. Foulkes, S. Kaye, *Prog. Retin. Eye Res.* **2022**, *89*, 101031.

[4]   Y. Zhang, Y. Yu, G. Li, X. Zhang, Z. Wu, L. Lin, *Biomacromolecules* **2021**, *22*, 2020.

[5]   J. W. Lee, T. Somerville, S. B. Kaye, V. Romano, *J. Clin. Med.* **2021**, *10*, 758.

[6]   A. Austin, T. Lietman, J. Rose-Nussbaumer, *Ophthalmology* **2017**, *124*, 1678.

[7]   V. S. Chang, D. K. Dhaliwal, L. Raju, R. P. Kowalski, *Cornea* **2015**, *34*, 698.

[8]   C. Yu, Y. Gao, Y. Y. Zhang, J. Wang, Y. Y. Zhang, J. Li, X. X. Zhang, Z. Wu, X. X. Zhang, *Biomacromolecules* **2021**, *22*, 3704.

[9]   A. F. Durrani, S. Atta, A. K. Bhat, A. Mammen, D. Dhaliwal, R. P. Kowalski, V. Jhanji, *Am. J. Ophthalmol.* **2020**, *214*, 119.

[10]   H. Han, Y. Gao, M. Chai, X. Zhang, S. Liu, Y. Huang, Q. Jin, A. Grzybowski, J. Ji, K. Yao, *J. Control. Release* **2020**, *327*, 676.

[11]   W. Fan, H. Han, Z. Lu, Y. Huang, Y. Zhang, Y. Chen, X. Zhang, J. Ji, K. Yao, *Bioeng. Transl. Med.* **2023**, *8*, e10380.

[12]   H. J. Jian, R. S. Wu, T. Y. Lin, Y. J. Li, H. J. Lin, S. G. Harroun, J. Y. Lai, C. C. Huang, *ACS Nano* **2017**, *11*, 6703.

[13]   D. D. Nguyen, S. J. Lue, J. Y. Lai, *Colloid. Surface. B* **2021**, *205*, 111856.

[14]   D. D. Nguyen, L. J. Luo, J. Y. Lai, *Mater. Sci. Eng. C* **2021**, *119*, 111497.
45

[15] H. Y. Lin, S. W. Wang, J. Y. Mao, H. T. Chang, S. G. Harroun, H. J. Lin, C. C. Huang, J. Y. Lai, *Chem. Eng. J.* **2021**, *411*, 128469.

[16] Y. Huang, Y. Chen, Z. Lu, B. Yu, L. Zou, X. Song, H. Han, Q. Jin, J. Ji, *Small* **2023**, 2302578.

[17] H. Zhang, W. Jiang, Y. Peng, J. Yang, X. Chu, Z. Long, R. Li, Q. Liang, H. Suo, S. Wang, M. Yang, J. Qi, D. Ding, Y. W. Yang, B. Wang, *Biomaterials* **2022**, *286*, 121577.

[18] D. Li, Q. Liu, Q. Qi, H. Shi, E. Hsu, W. Chen, W. Yuan, Y. Wu, S. Lin, Y. Zeng, Z. Xiao, L. Xu, Y. Zhang, T. Stoyanova, W. Jia, Z. Cheng, *Small* **2020**, *16*, 2003851.

[19] W. Wang, Y. Kong, J. Jiang, Q. Xie, Y. Huang, G. Li, D. Wu, H. Zheng, M. Gao, S. Xu, Y. Pan, W. Li, R. Ma, M. X. Wu, X. Li, H. Zuilhof, X. Cai, R. Li, *Angew. Chem. Int. Ed.* **2020**, *59*, 22431.

[20] H. Liu, G. Hong, Z. Luo, J. Chen, J. Chang, M. Gong, H. He, J. Yang, X. Yuan, L. Li, X. Mu, J. Wang, W. Mi, J. Luo, J. Xie, X. D. Zhang, *Adv. Mater.* **2019**, *31*, 1901015.

[21] X. Song, W. Zhu, X. Ge, R. Li, S. Li, X. X. X. Chen, J. Song, J. Xie, X. X. X. Chen, H. Yang, *Angew. Chem. Int. Ed.* **2021**, *60*, 1306.

[22] Y. Kong, D. Santos-Carballal, D. Martin, N. N. Sergeeva, W. Wang, G. Liu, B. Johnson, B. Bhayana, Z. Lin, Y. Wang, X. Le Guével, N. H. de Leeuw, D. Zhou, M. X. Wu, *Mater. Today* **2021**, *51*, 96.

[23] Y. Zheng, J. Wu, H. Jiang, X. Wang, *Coord. Chem. Rev.* **2020**, *431*, 213689.

[24] X. Zhang, X. Chen, Y. W. Jiang, N. Ma, L. Y. Xia, X. Cheng, H. R. Jia, P. Liu, N. Gu, Z. Chen, F. G. Wu, *ACS Appl. Mater. Inter.* **2018**, *10*, 10601.

[25] D. Luo, X. Wang, S. Zeng, G. Ramamurthy, C. Burda, J. P. Basilion, *Small* **2019**, *15*, 1900968.

[26] P. Pei, W. Shen, H. Zhou, Y. Sun, J. Zhong, T. Liu, K. Yang, *Nano Today* **2021**, *38*, 101144.

[27] S. Varela-Aramburu, C. Ghosh, F. Goerdeler, P. Priegue, O. Moscovitz, P. H. Seeberger, *ACS Appl. Mater. Inter.* **2020**, *12*, 43380.

[28] V. Cagno, P. Andreozzi, M. D'Alicarnasso, P. Jacob Silva, M. Mueller, M. Galloux, R. Le Goffic, S. T. Jones, M. Vallino, J. Hodek, J. Weber, S. Sen, E. R. Janeček, A. Bekdemir, B. Sanavio, C. Martinelli, M. Donalisio, M. A. Rameix Welti, J. F. Eleouet, Y. Han, L. Kaiser, L. Vukovic, C. Tapparel, P. Král, S. Krol, D. Lembo, F. Stellacci, *Nat. Mater.* **2018**, *17*, 195.

[29] Y. Xie, Y. Y. Liu, J. Yang, Y. Y. Liu, F. Hu, K. Zhu, X. Jiang, *Angew. Chem. Int. Ed.* **2018**, *57*, 3958.

[30] M. Tang, J. Zhang, C. Yang, Y. Zheng, H. Jiang, *Front. Chem.* **2020**, *8*, 181.

[31] K. Zheng, M. I. Setyawati, D. T. Leong, J. Xie, *ACS Nano* **2017**, *11*, 6904.

[32] K. Kwak, D. Lee, *Acc. Chem. Res.* **2019**, *52*, 12.

[33] M. Zhou, R. Jin, *Annu. Rev. Phys. Chem.* **2020**, *72*, 121.

[34] Q. Shi, Z. Qin, S. Sharma, G. Li, *Chem. Rec.* **2021**, *21*, 879.

[35] M. G. Taylor, G. Mpourmpakis, *Nat. Commun.* **2017**, *8*, 15988.

47

[36] J. Lee, M. H. Naveen, J. Park, K. Pyo, H. Kim, D. Lee, J. H. Bang, *ACS Energy Lett.* **2021**, *6*, 2305.

[37] Y. Song, H. Abroshan, J. Chai, X. Kang, H. J. Kim, M. Zhu, R. Jin, *Chem. Mater.* **2017**, *29*, 3055.

[38] M. A. H. Muhammed, P. K. Verma, S. K. Pal, R. C. A. Kumar, S. Paul, R. V. Omkumar, P. Thalappil, *Chem. - Eur. J.* **2009**, *15*, 10110.

[39] M. Waszkielewicz, J. Olesiak-Banska, C. Comby-Zerbino, F. Bertorelle, X. Dagany, A. K. Bansal, M. T. Sajjad, I. D. W. Samuel, Z. Sanader, M. Rozycka, M. Wojtas, K. Matczyszyn, V. Bonacic-Koutecky, R. Antoine, A. Ozyhar, M. Samoc, *Nanoscale* **2018**, *10*, 11335.

[40] L. Tang, X. Kang, S. Wang, M. Zhu, *Langmuir* **2019**, *35*, 12350.

[41] M. P. Maman, A. S. Nair, A. M. Abdul Hakkim Nazeeja, B. Pathak, S. Mandal, *J. Phys. Chem. Lett.* **2020**, *11*, 10052.

[42] M. Hesari, M. S. Workentin, *J. Mater. Chem. C* **2014**, *2*, 3631.

[43] M. Rambukwella, N. A. Sakthivel, J. H. Delcamp, L. Sementa, A. Fortunelli, A. Dass, *Front. Chem.* **2018**, *6*, 330.

[44] T. C. Jones, L. Sumner, G. Ramakrishna, M. Bin Hatshan, A. Abuhagr, S. Chakraborty, A. Dass, *J. Phys. Chem. C* **2018**, *122*, 17726.

[45] Z. Pang, W. Yan, J. Yang, Q. Li, Y. Guo, D. Zhou, X. Jiang, *ACS Nano* **2022**, *16*, 16019.

[46] J. Lin, R. L. Rouseff, S. Barros, M. Naim, *J. Agric. Food Chem.* **2002**, *50*, 813.

48

[47] I. Blank, *ACS Symp. Ser.* **2002**, *826*, 25.

[48] R. López, N. Ortín, J. P. Pérez-Trujillo, J. Cacho, V. Ferreira, *J. Agric. Food Chem.* **2003**, *51*, 3419.

[49] World Health Organization, Sixty-eighth Meet. Jt. FAO/WHO Expert Comm. Food Addit., Geneva, **2008**.

[50] R. L. Smith, S. M. Cohen, J. Doull, V. J. Feron, J. I. Goodman, L. J. Marnett, P. S. Portoghese, W. J. Waddell, B. M. Wagner, T. B. Adams, *Food Technol.* **2005**, *59*, 24.

[51] S. Jiang, Z. Cao, *Adv. Mater.* **2009**, *22*, 920.

[52] Z. Pang, Q. Li, Y. Jia, W. Yan, J. Qi, Y. Guo, F. Hu, D. Zhou, X. Jiang, *Chem. Sci.* **2021**, *12*, 14871.

[53] A. Das, T. Li, K. Nobusada, C. Zeng, N. L. Rosi, R. Jin, *J. Am. Chem. Soc.* **2013**, *135*, 18264.

[54] Q. Yao, V. Fung, C. Sun, S. Huang, T. Chen, D. Jiang, J. Y. Lee, J. Xie, *Nat. Commun.* **2018**, *9*, 1979.

[55] L. Luo, Z. Liu, X. Du, R. Jin, *J. Am. Chem. Soc.* **2022**, *144*, 19243.

[56] Z. Wu, R. Jin, *Nano Lett.* **2010**, *10*, 2568.

[57] M. Lu, L. Su, Y. Luo, X. Ma, Z. Duan, D. Zhu, Y. Xiong, *Anal. Methods* **2019**, *11*, 4829.

[58] Y. Negishi, K. Nobusada, T. Tsukuda, *J. Am. Chem. Soc.* **2005**, *127*, 5261.

[59] S. Huo, Y. Jiang, A. Gupta, Z. Jiang, R. F. Landis, S. Hou, X. J. Liang, V. M.

Rotello, *ACS Nano* **2016**, *10*, 8732.

[60] Centers for Disease Control and Prevention, *Antibiotic resistance threats in the United States, 2019*, Atlanta, Georgia, **2019**.

[61] A. S. Lee, H. de Lencastre, J. Garau, J. Kluytmans, S. Malhotra-Kumar, A. Peschel, S. Harbarth, *Nat. Rev. Dis. Prim.* **2018**, *4*, 18033.

[62] C. Wölk, H. Youssef, T. Guttenberg, H. Marbach, G. Vizcay-Barrena, C. Shen, G. Brezesinski, R. D. Harvey, *ChemPhysChem* **2020**, *21*, 702.

[63] A. Müller, M. Wenzel, H. Strahl, F. Grein, T. N. V. Saaki, B. Kohl, T. Siersma, J. E. Bandow, H. G. Sahl, T. Schneider, L. W. Hamoen, *Proc. Natl. Acad. Sci.* **2016**, *113*, E7077.

[64] N. Cotroneo, R. Harris, N. Perlmutter, T. Beveridge, J. A. Silverman, *Antimicrob. Agents Chemother.* **2008**, *52*, 2223.

[65] R. M. Humphries, S. Pollett, G. Sakoulas, *Clin. Microbiol. Rev.* **2013**, *26*, 759.

[66] M. T. Lee, W. C. Hung, M. H. Hsieh, H. Chen, Y. Y. Chang, H. W. Huang, *Biophys. J.* **2017**, *113*, 82.

[67] H. W. Huang, *Biochim. Biophys. Acta - Biomembr.* **2020**, *1862*, 183395.

[68] M. T. Lee, P. Y. Yang, N. E. Charron, M. H. Hsieh, Y. Y. Chang, H. W. Huang, *Biochemistry* **2018**, *57*, 5629.

[69] G. Zhang, S. Li, K. W. Cheng, T. F. Chou, *Eur. J. Med. Chem.* **2021**, *219*, 113446.

[70] D. Frees, A. Chastanet, S. Qazi, K. Sørensen, P. Hill, T. Msadek, H. Ingmer,

Mol. Microbiol. **2004**, *54*, 1445.

[71]   J. K. Lithgow, E. Ingham, S. J. Foster, *Microbiology* **2004**, *150*, 373.

[72]   I. Chatterjee, S. Schmitt, C. F. Batzilla, S. Engelmann, A. Keller, M. W. Ring, R. Kautenburger, W. Ziebuhr, M. Hecker, K. T. Preissner, M. Bischoff, R. A. Proctor, H. P. Beck, H. P. Lenhof, G. A. Somerville, M. Herrmann, *Proteomics* **2009**, *9*, 1152.

[73]   N. A. Spahich, N. P. Vitko, L. R. Thurlow, B. Temple, A. R. Richardson, *Mol. Microbiol.* **2016**, *100*, 759.

[74]   F. V. Sena, F. M. Sousa, A. S. F. Oliveira, C. M. Soares, T. Catarino, M. M. Pereira, *Redox Biol.* **2018**, *16*, 209.

[75]   L. A. Schurig-Briccio, P. K. Parraga Solorzano, A. M. Lencina, J. N. Radin, G. Y. Chen, J. Sauer, T. E. Kehl-Fie, R. B. Gennis, *EMBO Rep.* **2020**, *21*, e45832.

[76]   Z. Liang, W. Liu, Z. Wang, P. Zheng, W. Liu, J. Zhao, Y. Zhong, Y. Zhang, J. Lin, W. Xue, S. Yu, *Acta Biomater.* **2022**, *143*, 428.

[77]   N. Singh, J. Rajwade, K. M. Paknikar, *Colloid. Surface. B* **2019**, *175*, 487.

[78]   Y. Zheng, W. Liu, Z. Qin, Y. Chen, H. Jiang, X. Wang, *Bioconjug. Chem.* **2018**, *29*, 3094.

[79]   L. Song, V. H. B. Ho, C. Chen, Z. Yang, D. Liu, R. Chen, D. Zhou, *Adv. Healthc. Mater.* **2013**, *2*, 275.

[80]   C. Ross, B. Syed, J. Pak, V. Jhanji, J. Yamaki, A. Sharma, *Pharmaceutics* **2021**, *13*, 289.

[81]   U. Ubani-Ukoma, A. Chauhan, G. Schultz, D. J. Gibson, *MethodsX* **2020**, *7*, 100876.

[82]   H. Jeong, J. H. Park, J. H. Shin, J. C. Yoo, C. Y. Park, J. Hong, *Chem. Mater.* **2018**, *30*, 8528.

[83]   F. Kretschmer, S. Sajgo, V. Kretschmer, T. C. Badea, *J. Neurosci. Meth.* **2015**, *256*, 91.